USGS Award Number: G19AP00102

Title of Award: Determination of slip rate along the southern Calico fault in the southernmost Eastern California Shear Zone, Mojave Desert, California

Authors:
James A. Spotila[1,2], Max M. Garvue[1], Michael Vadman[1], Sean Bemis[1], Lewis Owen[3], Paula Figueiredo[3]

[1]Department of Geosciences	[3]Dept. Marine, Earth and Atmospheric Sciences
Virginia Tech	NC State University
926 W. Campus Drive	2800 Faucette Drive, 1125 Jordan Hall
Blacksburg, VA 24061	Campus Box 8208
[2]P: 540-557-7682, F: none	Raleigh, NC 27695
[2]email: spotila@vt.edu	

Term Covered by the Award: 9/1/2019 - 8/31/2021

Abstract:
The Calico fault is one of the primary structures of the southern Eastern California Shear Zone (ECSZ). Although it has not ruptured in historical time, it has the highest apparent slip rate in the ECSZ and may be the key to understanding the difference between geologic and geodetic slip rates. We have mapped and measured a suite of offsets along the southern Calico fault, located approximately 40 km south of previous work within a difficult to access military installation. Field observations and remote mapping using high-resolution satellite imagery and topography (from UAV surveys) reveal a 5-km-long fault stretch with numerous clear, measurable offsets. Although cosmogenic nuclide ^{10}Be results have been delayed due to the COVID-19 pandemic, initial luminescence (OSL) ages suggest a preliminary slip rate of 4-5 mm/yr over the Holocene. The geomorphic interpretation of these offsets is non-unique, however. A robust slip rate will not be obtained until pending geochronology is available. We have also discovered a recent paleorupture along the combined Calico and Hidalgo faults. We mapped 18 km of a clear, semi-continuous surface rupture, which mimics the appearance of a degraded version of historical ruptures in the region. Average right-lateral offset of 2.2 m implies the paleorupture was longer than mapped. Based on scaling relationships, the paleorupture may have been >65 km long and equivalent to M7.2, comparable to the 1992 Landers earthquake. Offset stratigraphy dated using OSL in a paleoseismic trench also indicate the paleorupture occurred at 0.7-1.9 ka. It may thus connect with the most recent event (0.6-2.0 ka) on the Calico fault observed 55 km to the north (Ganev et al., 2010). This indicates the Calico fault has failed in complex, multi-fault ruptures, similar to historical events in the ECSZ. It also demonstrates that the linear extent and geometry of paleoruptures may be mappable beyond point data observed at individual trench sites.

This Final Report will form the basis of two manuscripts to be submitted for publication in an open literature, peer-reviewed journal.

Report:

1. Introduction and Background

        The Eastern California shear zone (ECSZ) poses a significant earthquake hazard to the heavily populated southern California region. It accommodates ~25% of Pacific-North America relative plate motion (Savage et al., 1990; 2001; Sauber et al., 1994; Dixon et al., 2000), has produced significant earthquakes in the past few decades (1992 Landers M_w7.3, 1999 Hector Mine M_w7.1) (Sieh et al., 1993; Trieman et al., 2002), affects the state of stress on the neighboring San Andreas fault system (Jaume and Sykes, 1992; King et al., 1994), and appears to be in a period of intensified activity (Nur et al., 1993; Rockwell et al., 2000; Ganev et al., 2010). Understanding seismogenesis in the ECSZ is difficult, however, given that it consists of a ~125 km wide zone of diffuse dextral shear involving numerous northwest-striking dextral faults that are separated by complex stepovers and zones of distributed deformation (Dibblee, 1961; Dokka and Travis, 1990a/b) (Figure 1).

        An intriguing characteristic of the ECSZ is the apparent discrepancy between geologically and geodetically determined rates of fault motion. Geodesy indicates that the southern ECSZ in the Mojave Desert accommodates 11-18 mm/yr of right-lateral shear (Savage et al., 1990; Sauber et al., 1994; Dixon et al., 2000; Gan et al., 2000; Miller et al., 2001; Meade and Hager, 2005; Spinler et al., 2010; McGill et al., 2015; Evans et al., 2016). In contrast, the sum of known dextral slip rates across individual faults in the southern ECSZ is 6.2 mm/yr (Oskin et al., 2008). Individual slip rates for the major faults are generally ~1 mm/yr, whereas rates for shorter, less prominent faults are likely to be <0.4 mm/yr based on less pronounced geomorphic expressions (Oskin et al., 2008). This apparent discrepancy in slip rates may be due in part to a viscoelastic effect of the 1992 and 1999 ruptures, which could have resulted in post-seismic increase in strain of several mm/yr (Dixon et al., 2003; Chuang and Johnson, 2011; McGill et al., 2015; Liu et al., 2015). The discrepancy may also be explained partly by off-fault deformation (vertical-axis rotation, fragmentation, microcracking, short subparallel shear zones, penetrative pure shear), which could accommodate as much as 40% of the total strain (Nelson and Jones, 1987; Oskin and Iriondo, 2004; Oskin et al., 2007; Titus et al., 2007; Shelef and Oskin, 2010; Johnson, 2013; Dolan and Haravitch, 2014; Herbert et al., 2014a/b; Milliner et al., 2015). It could also be explained by incomplete fault mapping, in that many branching strands and unmapped faults have not been studied and could account for some of the missing strain. Another possible explanation is the difference in time scale of measurement and the possibility that transient increase in strain rates has occurred (Peltzer et al., 2001; Dolan et al., 2007; Oskin et al., 2007; Gourmelen et al., 2011).

The Calico fault system (which includes the Hidalgo and Mesquite Lake faults) displays the greatest discrepancy between geologic and geodetically determined slip rates for any fault in the ECSZ. The central Calico fault has the highest geologically estimated slip rates in the ECSZ of 1.8±0.3 (Oskin et al., 2007; 2008), 1.4±0.8 (Selander, 2015), and 3.1-3.6±0.5 mm/yr (Xie et al., 2018) (all spanning 50-700 ka). In contrast, geodetically estimated slip rates range from ~2 mm/yr (McClusky et al., 2001; Meade and Hager, 2005), 7.6 mm/yr (Evans et al., 2016), to as high as 10.8 mm/yr (McGill et al., 2015). The possible ~4-7 mm/yr discrepancy in geologic and geodetic slip rates may be partly due to viscoelastic deformation in the mantle following the 1992 Landers and 1999 Hector Mine ruptures (McGill et al., 2015; Evans et al., 2016). The Calico fault lies in the 20 km wide space between these ruptures, which spanned 70 km along the Johnson Valley, Homestead Valley, Emerson, and Camp Rock faults in 1992, and 48 km along the Mesquite Lake, Bullion, Pisgah, and Lavic Lake faults in 1999 (Sieh et al., 1993; Treiman et al., 2002) (Figure 1). Because slip-rate interpretations from geodetic data are model dependent, however, it is unclear how much of the discrepancy is real or can instead be explained by factors, such as a historical strain transient or off-fault deformation. It is also possible that geologically determined slip rates are inaccurate, due to overestimation of age of offset features or other factors (Xie et al., 2018). All three geologic slip-rates along the Calico fault were determined along a ~15 km stretch in the northern Rodman Mountains (Figure 1, 2), yet the measured rates exhibit high variation. This variability may be due to a combination of non-steady rates and variation in time period of measurement, local structural complexity (i.e. slip rate gradients; multiple fault strands), or measurement inaccuracy.

In addition to its high apparent slip rate, other characteristics make the Calico fault one of the most prominent faults of the ECSZ. It connects to the Hidalgo fault in the south and the Blackwater fault in the north to form the longest (>140 km), most through-going structure of the Mojave (Oskin et al., 2007) (Figure 1). The Calico fault has the largest estimated net displacement of faults in the southern ECSZ: 8-9.8 km defined geologically (Dokka and Travis, 1990a; Glazner et al., 2000; Andrew and Walker, 2016), or up to 20 km (Hidalgo fault) defined using offset aeromagnetic features (Jachens et al., 2002). These estimates suggest 10-20% of the ECSZ slip budget has been accommodated by the Calico fault. The central section of the Calico fault has experienced 4 ruptures in 9,000 yr based on paleoseismology north of the Rodman Mountains (Ganev et al., 2010), suggesting it has a higher rupture frequency that most faults in the ECSZ (i.e. typically ~ 5 ka recurrence interval) (Rubin and Sieh, 1997; Rockwell et al, 2000; Rymer et al., 2002; Dawson et al., 2003; Madden et al., 2006). These aspects, along with its dominant role in accommodating regional strain, suggest the Calico fault is one of the most important faults in the southern ECSZ and may be the nexus of what may be evolving as a new integrated component of the San Andreas fault system (Dokka and Travis, 1990b; Nur et al., 1993; Li and Liu, 2006; Plattner et al., 2010).

Despite its obvious importance, only the northern half of the Calico fault has been studied in detail. Slip rate determinations and paleoseismic investigations have been focused in the central portion of the fault near the Rodman Mountains, as well as farther north along the Blackwater fault (Figure 1, 2). In contrast, the southern ~70 km of the Calico fault and subparallel strands it bifurcates into (e.g. Hidalgo fault) have not been studied, other than basic 1:62,500 scale geologic mapping by T. Dibblee (1964; 1966;

1967a/b). The only geologic slip rate estimate for any fault in its vicinity south of the Rodman Mountains is for the Mesquite Lake fault near Twentynine Palms, which shows evidence for ~0.7-0.9 mm/yr motion and typical earthquake frequency for the ECSZ (Madden et al., 2006) (Figure 2). No slip rate estimates or other studies have focused on the ~40 km long Hidalgo fault. In part, this lack of study of the southern Calico fault system is due to limited access to the Marine Corps Air Ground Combat Center (MCAGCC) (i.e. Twentynine Palms base), which encircles almost its entire extent (Figure 2). Thus, although the Calico fault is an apparent key to understanding the discrepancy between geologic and geodetic slip rates in southern California, the activity of most of the fault has previously gone uncharacterized.

In this study, we attempt to quantify the long-term geologic slip rate on the southern Calico fault, to determine whether slip rate is variable along-strike (e.g. decreases to the south) and to further constrain the discrepancy between geologic and geodetic estimates. We have mapped a suite of geomorphic offsets along the fault in the Galway Lake-Hidalgo Mountain area and collected preliminary geochronologic data to constrain ages of some offsets. During the course of geomorphic investigations, we also discovered an apparent historical paleorupture trace along the Calico-Hidalgo faults, which we then mapped in detail and trenched. In combination, this work yields the first slip-rate estimates for the southern Calico fault and identifies another example of a Holocene multi-fault rupture in the ECSZ.

2. Methods

Initial reconnaissance to identify potential slip rate sites involved detailed examination of the Calico and Hidalgo faults from the northern end of North Hidalgo Mountain to the southern end of Hidalgo Mountain using visible satellite imagery on GoogleEarth (Figure 3). During this assessment, as well as fieldwork associated with a parallel NSF project on transpression in the ECSZ, we discovered evidence for a recent paleorupture along the faults. We subsequently mapped these features in detail using both satellite imagery (at 1:500 or better) and in the field (see section 3.3). We walked over half of the mapped trace of the paleorupture and field-checked many other areas. Numerous offsets along the paleorupture were also measured and a suitable paleoseismic site was identified along the paleorupture of the Hidalgo fault on Hidalgo Mountain (Figure 3). We later hand-trenched at this location to constrain the age of the paleorupture (see section 3.4). Suitable sites for slip rate investigations were identified only along North Hidalgo Mountain (Figure 4b). We constructed a geomorphic/neotectonic map of a 5-km-long swath along the Calico fault in this area, to define the context of potential fault offsets (e.g. Figure 5). Mapping utilized high-resolution satellite imagery (~1:500) and extensive field observations. We also obtained high-resolution topography to facilitate geomorphic mapping using Structure from Motion photogrammetry using aerial photographs from a UAV (Figure 4bc). The extent of the resulting DEMs is limited, however, due to difficulty obtaining permission to use the UAV on the military installation (MCAGCC).   We mapped and characterized suitable fault offsets for the slip-rate study in detail in the field. This included characterization of alluvium and alluvial surfaces for provenance and age-proxy constraints (Table 1). Some offsets were surveyed in the field using standard techniques (tape measure, hand-held laser EDM). Others were measured using satellite images and high-resolution DEMs on GoogleEarth

and/or ArcGIS, because of the difficulty of visualizing features from the ground (e.g. the apex of convex fans). Higher resolution surveying of offsets using a total station or differential GPS has not yet been completed due to limited access days to active training areas (TAs) on the military installation. Available satellite imagery of the area is very high quality, however, making it possible to examine and carefully measure offset features even without the higher resolution surveying.

We applied ^{10}Be Terrestrial Cosmogenic Nuclide (TCN) surface age dating and Optically Stimulated Luminescence (OSL) burial age dating on alluvial deposits to obtain age constraints on offsets. Along older alluvial fans with a bedrock source, we collected surface boulders (n=15) and amalgamated clasts (n=7) using established techniques (Lal, 1991; Gray et al., 2014; Frankel et al., 2016; Hedrick et al., 2017; Xie et al., 2018). Boulders are considered a reliable candidate for single-source surface age dating when using established criteria (Gosse and Phillips, 2001). We used large granitic boulders (generally ≥1 m diameter) with low centers of gravity and stable bases that lacked evidence for having toppled. Boulders used had roughly level tops and lacked evidence for mass lost due to post-deposition weathering (i.e. were still rounded and exhibited extensive varnish). We chiseled multiple rock chips from the outer 5 cm of the boulder surface to generate a sample. Where possible, at least 5 boulders were collected to constrain the age of a single depositional surface. Some surfaces did not contain suitable boulders, however. Along these surfaces we collected amalgamated clasts of quartzite (white vein quartz, orange-stained metasedimentary quartzite, or quartz-rich leucogranite) from surface float. We collected clasts 1-5 cm diameter from the surface that exhibited surface varnish or basal oxidation indicative of having remained at the surface for a long period. We generally collected ~30 clasts per surface for each amalgamated sample, to combat the higher uncertainty of any individual clasts due to unknown origins and higher susceptibility to movement by erosion and sheet flow. Only quartz-rich clasts that could not have been derived from weathering of a neighboring larger rock on the alluvial surface were collected. Each amalgamated sample was then combined and crushed, separated, and chemically treated during processing. Finally, we collected one depth profile from an alluvial exposure of a younger offset fan, consisting of n=6 samples spaced at ~0.3 m depth (collected after digging back ~1 m into the vertical exposure). All TCN samples were crushed, sieved, separated, and chemically treated for quartz enrichment and ^{10}Be extraction at NCSU and are currently or soon-to-be analyzed by AMS at PRIMELAB. Of 28 samples collected for TCN dating, 12 have or will be analyzed and paid for using USGS funds (data are still pending), whereas the remainder will be analyzed using other funding. All TCN data are expected by early spring of 2022. Although most samples were collected within the first few months of this project (fall of 2019), delays in obtaining data resulted from the COVID-19 pandemic, which shut down the newly relocated Geochronology Laboratory at NCSU (formerly at U. Cincinnati) for over half a year and slowed subsequent progress due to personnel access limitations associated with newly imposed safety regulations.

We collected 13 OSL samples from younger deposits with high concentrations of quartz sand. These are limited to the northern slip rate areas along the Calico fault (n=5), where proximal alluvium is enriched in recycled quartz sand, and the paleoseismic trench on the Hidalgo fault (n=8). OSL samples were collected using standard techniques (Mahan et al., 2007; Owen et al., 2007; Rhodes, 2011; Roder et al., 2012), involving

pounding a sealed 5 cm diameter, 20 cm long steel tube into a discrete layer of fine to coarse sand that lacks pebbles and with clear bedding planes (to avoid uncertainties including partial bleaching from sediment mixing processes). Samples in natural exposures were taken at ~0.5 m depth after excavating back 20-30 cm. Tubes were extracted (once tightly-packed with sediment) without exposure to light (to avoid bleaching). OSL samples have been processed in a dark room and analyzed using standard techniques at NCSU. Uncertainties in OSL ages include partial bleaching from mixing of sediment due to possible bioturbation and pedogenic processes, although the sedimentary intervals sampled lacked obvious evidence for either process. Of the OSL samples collected, 12 have been dated using USGS funds (Table 2), whereas one sample collected more recently has not yet been processed.

3. Results

3.1 Mapped Offsets

The field sites for measuring slip-rate along the Calico fault are located 4 km north of the confluence with the Hidalgo fault and 40 km south of Xie et al.'s (2018) study location (Figure 2, 3). The study area consists of a series of offset alluvial surfaces and streams spread along a 5-km-long stretch of the Calico fault (Figure 3). The fault exhibits a sharp geomorphic expression that is easily identified on satellite imagery as well as the high-resolution topography in two structure-from-motion (SfM) DEMs we produced using UAV surveys (Figure 4bc). The fault is primarily located along the slope-break between displaced fan surfaces and uplifted alluvium and bedrock of a transpressional ridge (Northern Hidalgo Mountain) and is easily mapped based on a sharp lineament, deflected streams, shutter ridges, scarps, triangular facets, offset terraces, and other features. Within the area are several offset surfaces for which age constraints have been or will be obtained in the course of this project.

The Calico fault consists primarily of a single fault trace along North Hidalgo Mountain. The fault trace is relatively simple, but does exhibit a gentle restraining bend in the center of the region that is approximately 5-8° oblique to the overall orientation of the fault (N36°W) (Spotila and Garvue, 2021). This restraining bend occurs at the northern end of a series of bends in the Calico fault, which are responsible for uplift of three prominent, elongate ridges, the largest of which is Hidalgo Mountain (Figure 3). The gentle restraining bend in the study area has produced a broad plunging anticline on the eastern side of the Calico fault, which exposes a thick section of presumably Quaternary alluvium (Qof; Dibblee, 1966). In the northern slip-rate area (Figure 5), the fault juxtaposes young alluvium on the west against the older Quaternary alluvium (Qoa) on the east, such that the relief of the transpressional ridge is muted. To the south, however, the basement core of the anticline is exposed, such that the transpressional ridge has greater relief (Figure 3). This difference in the composition of the source area for offset younger alluvial fans to the west (i.e. basement vs. older Quaternary alluvium) translates to significant differences from north to south in geomorphology and surface characteristics of the displaced units.

The northernmost mapped region contains two offsets from which we have assessed slip-rate (see geomorphic maps in Figure 5 and 6). The Calico fault in this area has a sharp, easily followed geomorphic expression. The fault sharply truncates the older

6

Quaternary alluvium (Qoa) of the anticline to the east, forming a series of faceted spurs that are dissected due to the erodible nature of the older alluvium. Evidence for the fault's location includes a sharp continuous lineament on satellite imagery and high-resolution topography, meter-scale shutter ridges, deflected streams, a rounded fault scarp in young alluvium (Qa2), and well-defined 2-3-meter-wide zone of pinkish-gray fault gouge that outcrops in numerous locations where neotectonic mapping suggests the presence of recent faulting (Figure 7). The young alluvium on the west side of the fault consists of clasts and sand that are recycled from the older Quaternary alluvium (Qoa). Because Qoa was deposited in the center of a large basin we presume was sourced from the neighboring Bullion Mountains more than 5 km to the east, it has a high concentration of sand and well-rounded clasts. As a result, the recycled younger alluvium is sandier and more arkosic than what is observed for piedmont alluvium proximally-sourced from the basement-cored transpressional ridge farther south.

The first dated offset in the northern region (Offset #1) consists of an offset channel margin. East of the fault, this channel margin separates eroding Qoa in the plunging fold from the active wash (Qa1) and forms a clear linear feature that intersects the fault with a sharp piercing point (Figure 5). The eastern channel margin is unlikely to have been significantly modified by erosion since inception of offset, given the highly indurated character of Qoa and its significant topographic relief. To the west of the fault, the channel margin is manifest as a riser in a terrace of older, incised late Quaternary alluvium, Qa3 (Figure 5). The characteristics of this Qa3 alluvium and its tread surface are provided in Figure 8a (surface S1) (Table 1). The linear continuity and parallelism of the terrace riser in Qa3 and the channel margin to the east of the fault support the interpretation that the feature has been offset with only minor subsequent modification by erosion. Minor erosion and northward migration of the riser is locally evident, however, where the riser is slightly embayed and thus concave to the south (Figure 5c, 9). We minimized the effective of post-offset erosional modification in our reconstruction by projecting promontories in the riser to the fault to establish the northern piercing point, which required projection of the reconstructed riser over a ~13 m distance near the fault where the riser is not preserved (Figure 5a). Because these promontories form a straight line, we believe that they have largely been preserved from erosion since inception of offset from the canyon. However, we acknowledge that some erosion is possible, which would lead to an overestimate in the magnitude of slip using this terrace riser. We measured the dextral separation between the resulting piercing points in the field (on several occasions involving different observers) using a tape measure to be 19.2±2 m. The piercing points were also reconstructed and measured as 20.0±2 m using combined satellite imagery and high-resolution topography from SfM on GoogleEarth. We adopt the average of the field measurements to be the offset magnitude at this location (19.2±2 m), based on the local geomorphic conditions that enabled good field visualization. After restoration by this amount, the terrace riser aligns perfectly with the channel margin to the east. Other channels to north and south also match back up following reconstruction of the offset, as seen in the high-resolution topography (Figure 5c). The maximum age of this offset is constrained via the depositional age of Qa3 in the terrace as measured using OSL dating (see below). Because there is no constraint on the duration of time between deposition of Qa3 and the formation of the channel margin or the onset of its offset along the fault, the resulting estimate of slip rate may be an underestimate (see below).

The second dated offset in the northern region (Offset #2) consists of a similar offset magnitude of another Qa3 alluvial fan (Figure 6). Although we originally speculated that this fan was older based on its incised character and that it restored ~150 m to the larger canyon to the south (Canyon B), the characteristics of the alluvium and its geomorphic surface are comparable to the Qa3 fan of Offset #1 (surface S2, Figure 8a, Table 1), thereby suggesting similar age and smaller offset magnitude. This interpretation is supported by OSL dating (see below). Given the younger age of this fan, we interpret that it has likely been displaced a much shorter distance from Canyon A (Figure 6). Although the fan is dissected and only partially preserved, it exhibits an overall convex form with an approximate apex that is slightly shifted to the north relative to the outlet of Canyon A. We defined the fan apex using SfM high-resolution topography and restored it back to the center of Canyon A to obtain an estimate of the fan's offset, which we measured on GoogleEarth (average of 5 measurements) as 21.0±3 m (a to a', Figure 6). Given that the center of the fan has now been removed by erosion and the possibility that the apex once lied farther south, we also measured the offset by defining a 50-m-wide apex region of the fan and restoring its centerpoint to the center of Canyon A, resulting in a 14.0±4 m offset. A similar measure of offset (21.0±4 m) is obtained by restoring the eroded Qa3 riser to the south to intersect the dynamic edge of the modern Qa1 wash (i.e. continually adjusted during the course of offset accumulation), denoted by line X on Figure 6 (b to b'). The "Col1" deposit (young colluvium) that projects into the mouth of Canyon B is interpreted to be younger than the offset (i.e. continually building as the offset pushes the riser to the north and shields it from Qa1 deposition). Similarly, a secondary, possible-Qa3 fan a short distance to the north restores 18.5±4 m back to the center of Canyon C (c to c', Figure 6). Several other geomorphic features also appear to align well after restoration of 21 m offset, including the margin of another Qa3 fan to the north (d') and the margin of a Qa2 deposit with the position of a ridge at the opening of Canyon B (e') (Figure 6), although we deemed neither of these to be sufficiently defined to measure. We take the mean of the four measurements (18.6±4 m) to be a rough estimate of the right-lateral offset of this fan from its source. Although none of the specific offsets are individually well constrained, the suite of measurements appears to offer at least a viable reconstruction of the post-Qa3 right lateral offset at this location. The maximum age of this offset is constrained via the depositional age of Qa3 in the terrace as measured using OSL and TCN dating (see below). Because there is no constraint on the duration of time between deposition of Qa3 and the formation of the offsets, however, the resulting estimate of slip rate may be an underestimate (see below).

The southernmost mapped region contains of a suite of measured offsets and dated alluvial surfaces (satellite image and high resolution DEM shown in Figure 10; geomorphic map in Figure 11). The Calico fault exhibits a sharp trace and many indicators of recent activity, including small channel offsets, meter-scale offset shutter ridges, truncated alluvial units, and a soft path in young colluvium suggestive of recent rupture (see below). The fault juxtaposes the bedrock-cored ridge against a high piedmont consisting of older Qa6 fan surfaces. These surfaces are steeply inclined (~8°) and incised, in part due to buttressing by elevated knobs of an older presumed Quaternary mega-gravel debris deposit (Qodb) that occur in the valley west of the fault. The resulting drainages are clearly displaced by the fault (Figure 11). Four well-defined beheaded gullies appear to restore back to large source canyons, which define offsets of 59±3 m,

52±3 m, 49±2 m, and 50±3 m (as measured using GoogleEarth, each based on multiple measurement points), for an average of 52.5±3 m dextral offset (Figure 11a). Restoration of this offset reveals topography that lines up visually well based on the high resolution SfM topography (Figure 10). The maximum age of this offset should be constrained by the depositional age of Qa6c that forms an old alluvial surface overlying Qodb, which was deposited, then incised by Canyon A, and then offset. We have collected three amalgamated surface quartz samples and seven large boulders for TCN exposure age dating from the Qa6c deposit (see below). Characteristics of the Qa6c surface and alluvium are virtually identical on either side of the fault (surfaces S3 and S4), suggesting that that they were deposited as a single alluvial/debris flow sheet prior to offset (Figure 8b, 10b). These characteristics also indicate that Qa6c is much older than the Qa3 deposits to the north (Figure 8; Table 1). Several larger offsets are also evident at this location. A canyon incised into older alluvium (Qa6b) restores 74±5 m (GoogleEarth measurement) back to Canyon B, although this offset is not clearly datable. The Qa6b fan also restores to the narrow Qa6b deposit within Canyon B ~100±10 m (GoogleEarth measurement). The maximum age of this offset should be more narrowly constrained (i.e. than the 74 m offset) by the depositional age of Qa6b. Characteristics of the Qa6b surface and alluvium are very similar on either side of the fault (surfaces S5 and S6), suggesting that they may have been deposited as a single alluvial/debris flow unit prior to incision and offset (Figure 8c, 10c). We have collected four amalgamated surface quartz samples to date this Qa6b alluvial surface (see below) (Figure 11a). Additional age constraints on the Qa6 series of alluvium in this area will be obtained from exposure ages on eight large boulders on the Qa6a surface (Figure 11a). Characteristics of Qa6a suggest that it may be younger than either Qa6b or Qa6c, yet the presence of many large, datable boulders on the surface led us to sample as a means of further constraining the general timing of Qa6 deposition in the region. Although TCN ages are not available at the time of this report, we are hopeful that these ages will soon provide important control on the slip rate of the Calico fault in this area.

A final well-defined offset occurs between the northern and southern mapped regions (Figure 12). The Calico fault along this central stretch is less obvious than to the north and south, in part due to the rough terrain and because the fault cuts higher up on the colluvium-mantled bedrock hillslope. A shutter ridge of bedrock (location a) appears to have been cut through by incision of a large canyon (Canyon A), resulting in shifting of the main outlet stream. The drainage area of Canyon A is large (1.28 km^2), providing larger stream power than most other drainages along the ridge. Confounding the setting, it appears that local base level has dropped during the accumulation of offset of the shutter ridge. Prior to capture and incision of the shutter ridge and shifting of the outlet stream, a sheet of older alluvium (Qa4) was deposited continuously across both the bottom of Canyon A east of the fault and as a large fan west of the fault. This Qa4 unit is a distinct buff color on the satellite image and contains a large fraction of recycled sand from eroding Qoa, which makes up ~4/5 of the Canyon A drainage (Figure 12). The depositional surface of Qa4 now sits ~7 m above the modern wash and Qa1 deposit (Figure 12b), which are incised into an inner gorge that cuts through the shutter ridge (location b). Prior to formation of the inner gorge, an intermediate stage of incision occurred, which lowered the active drainage to the height of the abandoned and beheaded stream at location c. We interpret that a lower sheet of alluvium (Qa3), which forms an

intermediate tread, was then deposited from the stream at location c. Deposition of Qa3 may have continued after initial breaching of the shutter ridge at location b, based on the presence of Qa3 in narrow gorge. It is not clear whether the drop in base level from Qa4 to Qa1 was due to repositioning of the main channel from the apex to the flank of the Qa4 fan, or if it resulted in part from fluctuations in sediment supply and dynamics upstream (the Qa4 and Qa1 alluvial surfaces merge farther downstream). Restoration of ~20 m dextral offset repositions the abandoned channel (location c) with a subsidiary channel at the height of the Qa3 surface upstream (location d), as well as lining up the sharp northern margin of the inner gorge (e to e'). A large gap in the shutter ridge (location f) appears to ruin the reconstruction, but we interpret this gap to have occurred during accumulation of offset by rapid erosion in the inner gorge. Depositional age of the Qa4 alluvium should provide a maximum age for the accumulation of this offset on the fault. We have collected one sample for OSL dating, for which results are not yet available (see below). Characteristics of the Qa4 surface and alluvium are comparable to those of Qa3 farther north (S1 and S2) (Table 1), so it may end up being similar in age and thus consistent with having a similar magnitude of offset.

3.2 Geochronology and Preliminary Slip Rates

So far we have only obtained preliminary age control on offsets along the Calico fault described above. Ages for 12 OSL samples (eight of which correspond to the trench study, see below) have been obtained thus far at NCSU (Table 2). An additional OSL sample (CF6-OSL1, Figure 12) has yet to be processed.

We have also collected samples for terrestrial cosmogenic nuclide (TCN) surface exposure dating. We have collected 15 boulder samples from the southern slip rate area (Figure 11). Boulders sampled are generally >1 m diameter and were selected on the basis of their apparent stability on the alluvial surface (i.e. low center of gravity, no evidence for toppling) and lack of weathering or fracturing (i.e. retain original rounded surface) (Figure 13a). Many porphyritic monzonite boulders from the alluvial surfaces in the southern slip rate area were too weathered to sample. The boulder samples collected thus far have been crushed and sieved and have undergone dissolution and chemical treatments to isolate [10]Be at NCSU. The samples have taken longer than expected due to low quartz yield in the monzonite. Samples are nearly complete, however, and ages are pending soon from PRIMELAB (five of the boulders are being analyzed using USGS funds). We have also collected 7 amalgamated surface quartz clasts (vein or metasedimentary quartzite, generally n~30) from surfaces in the southern slip rate area (Figure 11; 13c). These samples are being analyzed using USGS funds and we are expecting data very soon from which we can calculate exposure. Finally, an additional 6 samples are being processed for [10]Be for a TCN depth profile at fan CF3 (Figure 6; 13b). These samples are also taking unexpectedly long due to difficulties obtaining pure quartz, but should be analyzed soon. Once completed, 28 TCN analyses will be utilized in this study, of which this grant is paying for 12 (others will be dated using independent funds). These analyses will provide ages for six offset alluvial surfaces for the slip rate study.

Preliminary slip rates can be calculated from the OSL ages that have been obtained thus far. The northernmost offset terrace riser (surface S1, Figure 5) has been dated with one OSL age (CF5OSL1) as 4.7±0.4 ka (Table 2). Based on the 19.2±2 m offset, this implies a slip rate of 4.1±0.8 mm/yr. The next offset fan to the south (surface

S2, Figure 6) has been dated with one OSL age (CF3OSL1) as 3.6±0.3 ka (Table 2). Based on the 18.6±4 m offset, this implies a slip rate of 5.2±1.5 mm/yr. The ages of these two deposits are similar and thus consistent with observed characteristics, including nearly identical percentage of weathered clasts, color of B_T horizon, and degree of oxidation of surface clasts (Figure 8a, Table 1). These ages are also considered minimum constraints on the ages of the offsets, given that the intervals of time between deposition and offset of the geomorphic features are not constrained. The inset, lower alluvium near surface S2, dated as 2.1±0.2 ka (CF4OSL1), cannot be used to date an offset but does provide additional control on the rate of deposition and aging of surfaces, and is thus consistent with the older age of the offset fan (Table 2).

No ages are yet available to constrain the timing of offsets in the southern slip rate area (Figure 11). Assuming a slip rate of 4 mm/yr, the 52.5 m average offset in this area would have accumulated in only ~13 ka. The characteristics of the offset alluvial surfaces S3 and S4 indicate much older ages than those of the Qa3 surfaces to the north (S1, S2) (Figure 8, Table 1). The S3 and S4 surfaces have over 40% weathered clasts, redder B_T horizons, deeper oxidation of clasts at the surface, pedogenic carbonate (possible stage III), and well developed pavement (lag gravel) with moderately well developed varnish (Table 2). As such, these surfaces may be older than ~20 Ka, based on comparison with other Mojave soils (Schlesinger, 1985; Wells et al., 1987). This could indicate a lower slip rate for this offset, or a greater interval of time between the formation of the alluvial surface (to be dated) and the incision of the offset canyon and formation of the terrace riser (Figure 11). By contrast, surfaces that bracket the 100 m offset to the north (S5 and S6) exhibit slightly younger characteristics than S3 and S4 (Figure 8, Table 2). At 4 mm/yr, these surfaces would be expected to be ~25 ka, which may be possible. Constraints from TCN exposure ages will thus be critical for assessing the slip rate based on offsets in the southern mapped area.

3.3 Paleorupture

To identify offsets for the slip rate study, we created a neotectonic map of the Calico and neighboring faults using a combination of satellite imagery and field observations. During this mapping we observed that certain lengths of the Calico and Hidalgo faults exhibit much sharper and more continuous geomorphic expressions, which suggests discrete, recent rupture activity. Subsequent observations support the interpretation that a distinct, mappable paleorupture occurs in the region. Given the importance of such a rupture to quantifying the late Quaternary activity of the Calico fault, we mapped and characterized this paleorupture in detail. Although outside of the scope of the original USGS grant as well as our parallel NSF Tectonics project focused on transpression in the ECSZ (e.g. Spotila and Garvue, 2021), the investigation of the paleorupture was deemed of value to both initiatives.

The paleorupture was initially identified and mapped using satellite imagery on the GoogleEarth viewer at ~1:500. We observed and mapped continuous, anastamosing, light-colored, thin lineaments that followed the general location of the original mapped fault trace. The lineaments appear strikingly similar to nearby historic surface rupture traces, such as from the 1999 Hector Mine earthquake (Figure 14). The lineaments are also readily discerned from vehicle tracks or footpaths based on geometry. Lineaments classified as paleorupture are single-track, follow steep V's in drainages rather than

11

following contours, do not meet and branch like networks of continuous paths, and show no relationship to other anthropogenic features (e.g. prehistoric rock circles or features associated with US Marine Corps training). Lineaments were easiest to identify in uplifted older piedmont surfaces, where a surface rupture would likely be better preserved (i.e. older surface, more cohesive and with erosion-resistant pavement). The lineaments are generally not mappable across areas of high sand concentration (e.g. eolian) or active alluvial washes, although locally can be traced through young alluvium or colluvium-covered piedmont surfaces. Where mapped, roughly half (44%) of the mapped paleorupture is well defined by lineaments, whereas the remainder had to be inferred where crossing younger alluvial surfaces or where lost on steeper, rubbly slopes (Figure 15a).

Field observations strengthen the interpretation that the mapped lineament is a continuous, single-generation paleorupture. Where well preserved on alluvial surfaces with good pavement, the lineament is expressed as a single-track, with a narrow zone (0.5-1 m) of loose disturbance, in which the pavement and colluvial surfaces have been disarticulated and are thus softer and broken, reminiscent of a degraded mole track (Figure 15bc). This zone is readily distinguished by the lack of good pavement, irregular consistency, and higher concentration of fines and associated denser ephemeral vegetation. In places this zone corresponds to a small scarp (<0.5 m high) or a convex break in slope. This zone of disturbance is visibly continuous as a mappable trace across older geomorphic surfaces in the field (Figure 16a-d). The paleorupture is readily distinct from recent and presumed prehistoric footpaths, which tend to consist of narrow troughs (0.1-0.2 m), are harder packed (not softer), are smoother due to manual removal of obstructions, and closely follow the microtopography (i.e. around boulders, contour in and out of gullies, and avoid steep talus slopes where walking is unreasonable). The link between the lineament and faulting can be locally confirmed where the feature is crossed by gullies that exhibit riser exposure, in which pulverized bedrock, shearing, and near-vertical fault gouge are observed (Figure 15a).

Geomorphic evidence of the paleorupture is mappable for a total length of ~18 km and is distributed along both the Calico and Hidalgo faults. Our final map of the paleorupture is presented in Figure 17, in which orange traces indicate where we directly mapped the feature in the field (58% of its length) and green traces represent where it was mapped only using satellite imagery due to difficulty of access. Darker fault traces indicate where the paleorupture is well defined by evidence, whereas lighter fault traces indicate where the fault was difficult to identify and therefore inferred between better preserved locations. The paleorupture is less well constrained along the Calico fault on the northeast flank of Hidalgo Mountain and on an east branching strand of the Hidalgo fault on North Hidalgo Mountain (Figure 17). In these areas the rupture appears less continuous and less fresh, and may reflect poorer preservation in rough terrain or may represent an older (separate) paleorupture. The paleorupture is most clearly defined on the Calico fault from the northern end of North Hidalgo Mountain (west flank) and along the east flank of Central Hidalgo Mountain and along the Hidalgo fault along the west flank of Hidalgo Mountain. The paleorupture is lost in the north along North Hidalgo Mountain, where piedmont surfaces are sandy due to recycled sand from older Qoa deposits that form the plunging anticline of the ridge. The paleorupture is similarly lost south of Hidalgo Mountain where the young alluvium of the valley has a significant

eolian sand content. Given that these end points are likely defined by preservation limits, we believe that the rupture likely continued farther to both the north and south.

Displacement along the paleorupture is almost exclusively dextral strike-slip. The rupture trace exhibits a rule-of-V's pattern that indicates a near-vertical geometry, and is similarly near vertical in exposures (Figure 15a). We measured 35 right-lateral offsets with minimal vertical displacement along the paleorupture (Table 3, Figure 17b). Offset features measured were typically ephemeral gullies, shutter ridges of colluvium, spur ridges, and lobe deposits (Figure 16e-h). These right-lateral offsets vary from 0.7-5.5 m, but are typically ~1-2 m (Figure 18). Some larger offsets may be due to multiple events (Figure 17b). We assigned errors to each measurement based on the geomorphic context, which we estimate to represent 2σ uncertainty. The minimum, maximum, and preferred measurements for each offset were used to calculate triangular probability distributions, which we then summed to construct a Cumulative Offset Probability Distribution (COPD) plot (Figure 18). The largest peak on the COPD is 2.3 m, which is our best estimate of the average slip for the mapped extent of the paleorupture. Other peaks at 6 and 9 m may represent multiple events based on their magnitude (i.e. exceeding those of other ECSZ historical ruptures) and the decrease in geomorphic freshness with larger offsets. The resulting variation (running average=2.31 m) in offsets <6 m (n=28) along the paleorupture length exhibits a typical variation for displacement along a strike-slip rupture (Figure 18b) (McGill and Rubin, 1999; Gold et al., 2013). The average of these 28 offsets is 2.18±0.45 m (3σ), based on a bootstrapping analysis (run 10,000x).

Assuming this 2.2 m average offset for the paleorupture, an empirical scaling relationship for average displacement suggests the event had moment magnitude (M) of 7.2 (Wells and Coppersmith, 1994). An event of this size would in turn be expected to have a 67 km long surface rupture based on similar scaling (Wells and Coppersmith, 1994). This implies that the paleorupture extended well beyond the endpoints of our 18 km mapped length of where it is preserved. If correct, this would make the paleorupture of the combined Calico-Hidalgo faults of similar size to the 1992 Landers earthquake and larger than the 1999 Hector Mine earthquake.

3.4 Paleoseismic Investigation of Paleorupture

Because of the obvious importance of the newly discovered paleorupture for seismogenesis of the ECSZ, we expanded our work to include a paleoseismic investigation of its timing. We trenched the paleorupture on the Hidalgo fault in the southwestern flank of Hidalgo Mountain (Figure 17). The location occurs partway up the mountain (elev. 998 m), where the Hidalgo fault cuts across mixed terrain including moderately sloping debris fans with good pavement and more rugged colluvial slopes. Numerous shutter ridges and small pressure ridges have generated small uphill-facing scarps, one of which has been the site of fine sediment deposition that overlaps the fault trace (Figure 15c). Two traces of the Hidalgo fault bound the resulting sediment-filled depression. We hand-excavated two ~1.5 m deep trenches (4 m and 9.5 m long) across the faults. The trenches do not connect due to an intervening deposit of coarse, immovable boulders, but span nearly the entire width of the sediment-filled depression (Figure 19a).

Trench T1 (east) consists of well-sorted fine-grained deposits with interspersed, matrix-supported, semi-angular cobbly layers (e.g. Layer T1-D) (Figure 19b). These

cobbly layers thin towards the trough center to the west, away from the slope. These hanging wall units sit against the footwall at the western edge of the trench and appear truncated and offset by fractures. The footwall is poorly sorted, matrix supported cobble talus (Unit T1-E). Well-sorted fine-grained deposits (Layer T1-C, B, and A) drape over the faulted T1-D layer and are inferred to have filled the open fracture produced by the surface rupture. Faults defined by textural and mechanical variations in the fine-grained deposits appear to cut through the basal layer (Layer T1-C), but do not penetrate Layer T1-B. This suggests that the most recent rupture postdates Layer T1-C, whereas Layer T1-C infilled an open fracture produced by the penultimate rupture.

Trench T2 (west) exposes horizontally bedded fine-grained sediments draped over a gently west-dipping cobble-boulder deposit (Figure 19c). T2 units are differentiated largely through textural differences. Faulting is found in the very western edge of T2, where fine-grained units are juxtaposed by fractures against poorly-sorted, matrix supported pebble to cobble talus that comprises the footwall on the west. Layer T2-A appears to overlap and post-date faulting. Layer T2-B abuts and may be deformed by the fractures, implying it postdates the most recent event.

In summary, we find evidence for rupture in both trenches. At least one paleoearthquake is recorded, but a penultimate event is possible in Trench T1. Based on the shallow depth and stratigraphically high positions of the faulted units in each trench, it seems likely that both fault strands ruptured in the most recent event. It seems unlikely that two separate earthquakes, one on each strand, could have occurred in the small amount of time it took to deposit less than 20 cm of sediment. Because this sediment is also loosely bound and soft, it seems likely that it has not been exposed at the surface for a significant period of time. The age of the most recent paleorupture appears bracketed by OSL ages in Trench T2 (Figure 19c, Table 2). Layer T2-B is dated at 2.8±0.2 ka and is faulted, whereas Layer T2-A post-dates the paleoearthquake and is 0.9±0.1 ka or 0.5±0.1 ka (different mineral ages). This implies the paleorupture along the Hidalgo fault (and Calico fault) occurred between 2.8 and ~0.7 ka, making the event a late Holocene rupture. This is consistent with the 1.7 to 1.9 ka age of Layer T1-C in Trench T1, which is faulted and fills the surface fracture (Figure 19b, Table 2). Assuming this is the same rupture, it narrows the maximum age of the paleoearthquake to ~1.9 ka (i.e. the paleorupture occurred between 1.9 and 0.7 ka). Layer T1-B does not appear to be faulted, but the 2.4±0.1 ka OSL age of this layer is older than the ages of Layer T1-C and is therefore difficult to interpret. Additional sampling may be required to rectify this age and constrain the minimum age of the paleorupture in Trench T1.

4. Discussion and Conclusions

New constraints on the slip rate of the Calico fault system from this study should have important implications for the dynamics and hazards of the ECSZ, including the discrepancy between geologic and geodetic data. Because of the limited age controls that are currently available for the mapped geomorphic offsets, we feel that it is premature to explore the possible implications at length. Initial results are pointing to a slip rate of 4-5 mm/yr for the southern Calico fault, which is faster than observed geologically to the north (1.4-3.6 mm/yr; Oskin et al., 2007; 2008; Selander, 2015; Xia et al., 2018). If this initial rate is accurate, it would imply that the Calico fault accounts for more than half of the total strain observed geologically in the southern ECSZ during the Holocene. There

are several possible explanations as to why the southern slip rate could differ from previous measurements. For example, slip rate may vary along the fault, or specifically may increase towards the south. The concentration of slip along the main fault trace (versus more widely-distributed deformation) may also vary along-strike (could be higher in the south). It is also possible that slip is inhibited along the Rodman Mountains stretch of the Calico fault to the north due to complex structural interaction with the sinistral Manix fault and thrust transfer zones (Selander, 2015). Alternatively, long-term slip rates may instead be non-steady and accelerating towards the present (given that our offsets are smaller and span a shorter period). However, we consider the 4-5 mm/yr slip rate estimate to be speculative, because of the non-uniqueness of the geomorphic reconstruction of offsets (e.g. possibility of erosional modification and uncertainty in original, pre-offset form). More data points are necessary to build a suite of estimates from the complex geomorphic setting along North Hidalgo Mountain to corroborate initial results. These data should be available soon, as additional geochronologic data are obtained, but future work may also be required.

A second and unexpected result of this study is the discovery of a late Holocene paleorupture along the combined Calico-Hidalgo fault. Although the mapped length of this rupture is 18 km, it seems likely that the original rupture was longer and has been lost to erosion and surface change along-strike to the north and south. Based on the average ~2.2 m dextral offset of the rupture, the original rupture length may have been ~70 km and may have corresponded to a M7.2 earthquake (i.e. larger than the 1999 Hector Mine rupture and comparable to the 1992 Landers rupture, which it bisects). Our paleoseismic investigations show that this rupture event occurred during the interval of 0.7-1.9 ka, which overlaps with the 0.6-2.0 ka (most recent) event identified on the Calico fault at Newberry Springs by Ganev et al. (2010). Ganev et al. (2010) also measured a suite of offsets along fault that averaged 2 m, similar to our observations. Cursory examination of satellite imagery on GoogleEarth also indicates that the fault observed by Ganev et al. (2010) shows similar morphometric features as the paleorupture we have mapped in the south. Because our paleoseismic site on Hidalgo Mountain is 55 km south of the Ganev et al. (2010) site, it is conceivable that this was the same rupture event. We mapped the paleorupture an additional 6 km south of our paleoseismic location, suggesting that the rupture (if the same event, and length of 70 km) could have extended for an additional 5-10 km, distributed to either the south of our mapped endpoint or north of their paleoseismic site. Madden et al. (2006) identified another late Holocene event (from 2.7-7.4 ka, but likely 3.9-4.6 ka) along the Mesquite Lake fault to the south. We suggest that this is not likely the same event as we observe, given that it is slightly older and would require the rupture to continue an additional 26 km south of its mapped endpoint (and across a 5-km-wide restraining bend), resulting in a total rupture length of almost (or over) 90 km. Nonetheless, our observations, combined with those of Ganev et al. (2010), imply that the combined Calico-Hidalgo fault system experienced a large late Holocene multi-fault rupture similar to the three complex ruptures that have occurred in the ECSZ in recent decades (1992, 1999, 2019). This implies that complex, multi-fault ruptures may be the normal mode of operation in the ECSZ. Furthermore, our observations show that it may be possible to map Holocene paleorupture geometry along ECSZ faults within certain terrain, and that ruptures may retain obvious, continuous expressions for at least 1-2 Ka in a desert environment.

References

Andrew, J.E., and Walker, J.D., 2016, Path and amount of dextral fault slip in the Eastern California shear zone across the central Mojave Desert, Geol. Soc. Amer. Bull., B31527-1.

Chuang, R. Y., and Johnson, K. M., 2011, Reconciling geologic and geodetic model fault slip-rate dis- crepancies in Southern California: Consideration of nonsteady mantle flow and lower crustal fault creep. Geology, 39(7), 627-630.

Dawson, T. E., McGill, S., and Rockwell, T., 2003, Irregular recurrence of paleoearthquakes along the central Garlock fault near El Paso Peaks, California, J. Geophys. Res., 108, 2356.

Dibblee, T.W., 1961, Evidence of strike-slip movement on northwest-trending faults in Mojave Desert, California, U.S. Geol. Surv. Professional Paper 424-B, 197-198.

Dibblee, T.W., 1964, Geological map of the Rodman Mountains quadrangle, San Bernardino County, California, 1:62,500, USGS Misc. Geol. Investigations Map I-430.

Dibblee, T.W., 1966, Geological map of the Lavic quadrangle, San Bernardino County, California, 1:62,500, USGS Misc. Geol. Investigations Map I-472.

Dibblee, T.W., 1967a, Geological map of the Emerson Lake quadrangle, San Bernardino County, California, 1:62,500, USGS Misc. Geol. Invest. Map I-490.

Dibblee, T.W., 1967b, Geological map of the Deadman Lake quadrangle, San Bernardino County, Calivornia, 1:62,500, USGS Misc. Geol. Investigations Map I-488.

Dixon, T. H., Miller, M., Farina, F., Wang, H., and Johnson, D. , 2000, Present-day motion of the Sierra Nevada block and some tectonic implications for the Basin and Range province, North American Cordillera. Tectonics, 19(1), 1-24.

Dixon, T. H., Norabuena, E., and Hotaling, L., 2003, Paleoseismology and Global Positioning System: Earthquake-cycle effects and geodetic versus geologic fault slip rates in the Eastern California shear zone. Geology, 31(1), 55-58.

Dokka, R.K., and Travis, C.J., 1990a, Late Cenozoic strike-slip faulting in the Mojave Desert, California, Tectonics, 9, 311-340.

Dokka, R.K., and Travis, C.J., 1990b, Role of the Eastern California shear zone in accommodating Pacific-North America plate motion, Geophys. Res. Lett., 17, 1323-1326.

Dolan, J. F., Bowman, D. D., and Sammis, C. G., 2007, Long-range and long-term fault interactions in Southern California. Geology, 35(9), 855-858.

Dolan, J. F., and Haravitch, B. D., 2014, How well do surface slip measurements track slip at depth in large strike-slip earthquakes? The importance of fault structural maturity in controlling on-fault slip versus off-fault surface deformation. Earth and Planetary Science Letters, 388, 38-47.

Evans, E. L., Thatcher, W. R., Pollitz, F. F., and Murray, J. R., 2016, Persistent slip rate discrepancies in the eastern California (USA) shear zone. Geology, 44(9), 691-694.

Frankel, K.L., Owen, L.A., Dolan, J.F., Knott, J.R., Lifton, Z.M., Finkel, R.C., and Wasklewicz, T., 2016, Timing and rates of Holocene normal faulting along the Black Mountains fault zone, Death Valley, USA., Lithosphere, 8, 3–22.

Gan, W., Svarc, J., Savage, J., and Prescott, W., 2000, Strain accumulation across the Eastern California shear zone at latitude 36 30 N, J. Geophys. Res., 105, 16,229-16,236.

Ganev, P., Dolan, J., Blisniuk, K., Oskin, M., and Owen, L., 2010, Paleoseismologic evidence for multiple Holocene earthquakes on the Calico fault: Implications for earthquake clustering in the Eastern California shear zone, Lithosphere, 2, 287-298.

Glazner, A.F., Bartley, J.M., and Sanner, W.K., 2000, Nature of the southwestern boundary of the central Mojave Tertiary province, Rodman Mountains, California, Geol. Soc. Amer. Bull., 112, 34-44.

Gold, P.O., Oskin, M.E., Elliott, A.J., Hinojosa-Corona, A., Taylor, M.H., Kreylos, O., and Cowgill, E., 2013, Coseismic slip variation assessed from terrestrial lidar scans of the El Mayor-Cucapah surface rupture, Earth and Planet. Sci. Lett., 366, 151-162.

Gosse, J.C., Phillips, F.M., 2001, Terrestrial in situ cosmogenic nuclides: Theory and application, Quaternary Science Reviews, 20(14), 1475–1560.

Gourmelen, N., Dixon, T. H., Amelung, F., and Schmalzle, G., 2011, Acceleration and evolution of faults: An example from the Hunter Mountain–Panamint Valley fault zone, Eastern California. Earth and Planetary Science Letters, 301(1), 337-344.

Gray, H.J., Owen, L.A., Dietsch, C., Beck, R.A., Caffee, M.A., Finkel, R.C., and Mahan, S.A., 2014, Quaternary landscape development, alluvial fan chronology and erosion of the Mecca Hills at the southern end of the San Andreas Fault zone, Quaternary Science Reviews, 105, 66–85.

Hedrick, K.A., Owen, L.A., Chen, J., Robinson, A., Yuan, Z., Yang, X., Imrecke, D.B., Li, W., Caffee, M.W., Schoenbohm, L.M., and Zhang, B., 2017, Quaternary history and landscape evolution of a high-altitude intermountain basin at the western end of the Himalayan-Tibetan orogen, Waqia Valley, Chinese Pamir, Geomorphology, 284, 156–174.

Herbert, J., Cooke, M., Oskin, M., and Difo, O., 2014a, How much can off-fault deformation contribute to the slip rate discrepancy within the eastern California shear zone? Geology, 42, 71-74.

Herbert, J., Cooke, M., Marshall, S., 2014b, Influence of fault connectivity on slip rates in southern California: Potential impact on discrepancies between geodetic derived and geologic slip rates, J. Geophys. Res. Solid Earth, 119, 2342-2361.

Jachens, R.C., Langenheim, V.E., and Matti, J.C., 2002, Relationship of the 1999 Hector Mine and 1992 Landers fault ruptures to offsets on Neogene faults and distribution of late Cenozoic basins in the Eastern California shear zone: Bulletin of the Seismological Society of America, v. 92, p. 1592–1605.

Jaume, S.C., and Sykes, L.R., 1992, Changes in the state of stress on the southern San Andreas fault resulting from the California earthquake sequence of April to June 1992, Science, 258, 1325-1328.

Johnson, K., 2013, Slip rates and off-fault deformation in southern California inferred from GPS data and models, J. Geophys. Res., 118, 5643-5664.

King, G.C., Stein, R.S., and Lin, J., 1994. Static stress change and the triggering of earthquakes, Bull. Seism. Soc. Amer., 84(3), 935-953.

Langenheim, V., and Jachens, R., 2002, The Emerson Lake Body: A link between the Landers and Hector Mine earthquakes, southern California, as inferred from gravity and magnetic anomalies, Bull. Seism. Soc. Amer., 92, 1606-1620.

Lal, D., 1991, Cosmic ray labeling of erosion surfaces: in situ nuclide production rates and erosion models. Earth and Planetary Science Letters 104, 429-439

Li, Q., and Liu, M., 2006, Geometrical impact of the San Andreas fault on stress and seismicity in California, Geophys. Res. Lett., 33, L08302.

Liu, S., Shen, Z. K., and Bürgmann, R., 2015, Recovery of secular deformation field of Mojave shear zone in southern California from historical terrestrial and GPS measurements. Journal of Geophysi- cal Research: Solid Earth, 120(5), 3965-3990.

Madden, C., Rubin, C., and Streig, A., 2006, Holocene and latest Pleistocene activity on the Mesquite Lake fault, near Twentynine Palms, Eastern California Shear Zone: Implications for fault interaction, Seism. Soc. Amer. Bull., 96, 1305-1320.

Mahan, S.A., Miller, D.M., Menges, C.M., and Yount, J.C., 2007, Late Quaternary stratigraphy and luminescence geochronology of the northeastern Mojave Desert, Quaternary International, 166, 61-78.

Meade, B., and Hager, B., 2004, Viscoelastic deformation for a clustered earthquake cycle, Geophys. Res. Lett., 31, L10610.

McClusky, S. C., Bjornstad, S. C., Hager, B. H., King, R. W., Meade, B. J., Miller, M. M., and Souter, B. J., 2001, Present day kinematics of the eastern California shear zone from a geodetically con- strained block model. Geophysical Research Letters, 28(17), 3369-3372.

McGill, S. F., Spinler, J. C., McGill, J. D., Bennett, R. A., Floyd, M. A., Fryxell, J. E., and Funning, G. J., 2015, Kinematic modeling of fault slip rates using new geodetic velocities from a transect across the Pacific-North America plate boundary through the San Bernardino Mountains, California. Jour- nal of Geophysical Research: Solid Earth, 120(4), 2772-2793.

McGill, S.F., and Rubin, C.M., 1999, Surficial slip distribution on the central Emerson fault during the June 28, 1992, Landers earthquake, California, J. Geophys. Res., 104, 4811-4833.

Miller, M.M., Johnson, D., Dixon, T., and Dokka, 2001, Refined kinematics of the Eastern California shear zone from GPS observations, J. Geophys. Res., 106, 2245-2264.

Milliner, C., Dolan, J., Hollingsworth, J., Leprince, S., Ayoub, F., and Sammis, C., 2015, Quantifying near-field and off-faul deformation patterns of the 1992 Mw7.3 Landers Earthquake, Geochem., Geophys., Geosystems, 16, 1577-1598.

Nelson, M., and Jones, C., 1987, Paleomagnetism and crustal rotations along a shear zone, Las Vegas Range, southern Nevada, Tectonics, 6, 13-33.

Nur, A., Ron, H. and Beroza, G., 1993, The nature of the Landers-Mojave earthquake line, Science, 261, 201-203.

Oskin, M., and Iriondo, A., 2004, Large-magnitude transient strain accumulation on the Blackwater fault, Eastern California shear zone, Geology, 32, 313-316.

Oskin, M., Perg, L., Shelef, E., Strane, M., Gurney, E., Singer, B., and Zhang, X., 2008, Elevated shear zone loading rate during an earthquake cluster in eastern California, Geology, 36, 507-510.

Oskin, M., Perg, L., Blumentritt, D., Mukhopadhyay, S., and Iriondo, A., 2007, Slip rate of the Calico fault: Implications for geologic versus geodetic rate discpreancy in the Eastern California Shear Zone, J. Geophys. Res., 112, B03402, 16 p.

Owen, L.A., Bright, J., Finkel, R., Jaiswal, M., Kaufman, D., Mahan, S., Radtke, U., Schneider, J., Sharp, W., Singhvi, A., Warren, C., 2007, Numerical dating of a Late Quaternary spit-shoreline complex at the northern end of Silver Lake playa, Mojave

Desert, California: A comparison of the applicability of radiocarbon, luminescence, terrestrial cosmogenic nuclide, electron spin resonance, U-series, and amino acid racemization methods, Quaternary International, 166, 87-110.

Peltzer, G., Crampe, F., Hensley, S., and Rosen, P., 2001, Transient strain accumulation and fault interaction in the Eastern California shear zone, Geology, 29, 975-978.

Plattner, C., Malservisi, R., Furlong, K., and Govers, R., 2010, Development of the Eastern California Shear Zone - Walker Lane belt: The effects of microplane motion and pre-existing weakness in the Basin and Range, Tectonophys., 485, 78-84.

Rhodes, E.J., 2011, Optically stimulated luminescence dating of sediments over the past 200,000 years, Annual Review of Earth and Planetary Sciences, 39, 461-488.

Rockwell, T.K., Lindvall, S., Herzberg, M., Murbach, D., Dawson, T., and Berger, G., 2000, Paleoseismology of the Johnson Valley, Kickapoo, and Homestead Valley faults: Clustering of earthquakes in the Eastern California shear zone, Seism. Soc. Amer. Bulletin, 90, 1200-1236.

Roder, B., Lawson, M., Rhodes, E., Dolan, J., McAuliffe, L., and McGill, S., 2012, Assessing the potential of luminescence dating for fault slip rate studies on the Garlock fault, Mojave Desert, California, Quaternary Geochronology, 10, 285-290.

Rubin, C. M., and Sieh, K., 1997, Long dormancy, low slip rate, and similar slip-per-event for the Emerson fault, eastern California shear zone, J. Geophys. Res., 102, 15,319–15,333.

Rymer, M., Seitz, G., Weaver, K., Orgil, A., Faneros, G., Hamilton, J., and Goetz, C., 2002, Geologic and paleoseismic study of the Lavic Lake fault at Lavic Lake Playa, Mojave Desert, southern California, Seism. Soc. Amer. Bull., 92, 1577-1591.

Sauber, J. Thatcher, W., Solomon, S., and Lisowski, M, 1994, Geodetic slip rate for the eastern California shear zone and the recurrence time of Mojave Desert earthquakes, Nature, 367, 264-266.

Savage, J.C., Lisowski, M., and Prescott, W.H., 1990, An apparent shear zone trending north-northeast across the Mojave Desert into Owens Valley, eastern California, Geophys. Res. Lett., 12, 2113-2116.

Savage, J.C., Gan, W., and Svarc, J., 2001, Strain accumulation and rotation in the Eastern California Shear Zone, J. Geophys. Res., 106, 21,995-22,007.

Schlesinger, W.H., 1985, The formation of caliche in soils of the Mojave Desert, California, Geochimica et Cosmochimica Acta, 49, 57-66.

Selander, J. A., 2015, Mechanisms of Strain Transfer Along Strike-Slip Faults: Examples From the Mojave Desert, California. Ph.D Thesis, University of California, Davis.

Sieh, K., and 19 others, 1993, Near-field investigations of the Landers earthquake sequence, April to July, 1992, Science, 260, 171-176.

Shelef, E., and Oskin, M., 2010, Deformation processes adjacent to active faults: Examples from eastern California, J. Geophys. Res., 115, B05308, 24 p.

Spinler, J. C., Bennett, R. A., Anderson, M. L., McGill, S. F., Hreinsdóttir, S., and McCallister, A., 2010. Present-day strain accumulation and slip rates associated with southern San Andreas and eastern California shear zone faults. Journal of Geophysical Research: Solid Earth, 115, B11.

Spotila, J. A., and Garvue, M. M., 2021, Kinematics and evolution of thesouthern Eastern California shear zone, based on analysis of fault strike, distribution, activity, roughness, and secondary deformation, Tectonics, 40, e2021TC006859.

Titus, S.J., Housen, B., Tikoff, B., 2007, A kinematic model for the Rinconada fault system in central California based on structural analysis of en echelon folds and paleomagnetism, Journal of Structural Geology, 29, 961-982.

Treiman, J.A., Kendrick, K., Bryant, W., Rockwell, T., and McGill, S., 2002, Primary surface rupture associated with the Mw7.1 16 October 1999 Hector Mine earthquake, San Bernardino County, California, Seis. Soc. Amer. Bulletin, 92, 1171-1191.

Wells, D.L., and Coppersmith, K.J., 1994, New empirical relationships among magnitude, rupture length, rupture width, rupture area, and surface displacement, Bull. Seis. Soc. Am., 84, 974-1002.

Wells, S.G., McFadden, L.D., Dohrenwend, J.C., 1987. Influence of late Quaternary climate changes on geomorphic and pedogenic processes on a desert piedmont, eastern Mojave Desert, California. Quaternary Research, 27(2), 130-146.

Xie, S., Gallant, E., Wetmore, P.H., Figueiredo, P.M., Owen, L.A., Rasmussen, C., Malservisi, R., and Dixon, T.H., 2018, A new geological slip rate estimate for the Calico fault, eastern California: Implications for geodetic versus geologic rate estimates in the Eastern California Shear Zone, International Geology Review, 1-29.

Figure 1: Tectonic map of southern California imposed on topography showing the location of the Eastern California Shear Zone (ECSZ) (denoted by white dashed lines). The Mojave Block is defined by the Garlock, SAF, and NFTS, and Pinto Mountain faults. Gray lines indicate major active faults. Darker lines indicate the three large historical ruptures in the SECSZ. ETR = Eastern Transverse Ranges, NFTS = North Frontal Thrust System, SAF = San Andreas fault (SB = San Bernardino Strand, CV = Coachella Valley strand), SBM = San Bernardino Mountains, SGP = San Gorgonio Pass, SN = Sierra Nevada.
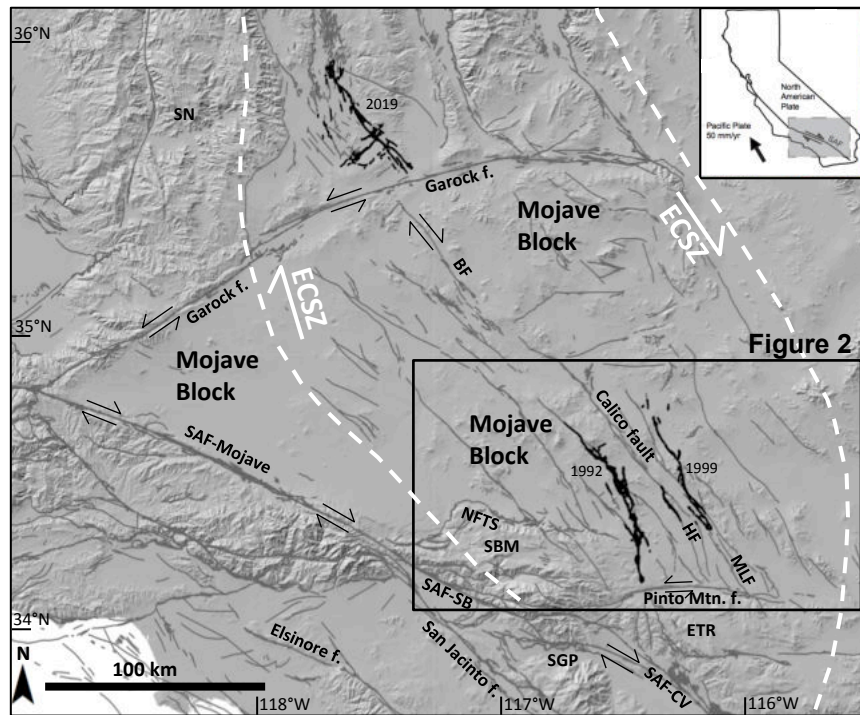
Figure 2: Fault map of the southern Eastern California Shear Zone (SECSZ) and the location of the Calico fault system (including the Calico, Hidalgo, and Mesquite Lake faults). Red box denotes location of Figure 3. Locations of previous studies on the Calico fault system are: A) Ganev et al., 2010; B) Xie et al., 2019; C) Oskin et al., 2007; D) Selander, 2015; E) Madden et al., 2006. Blue outline denotes the location of MCAGCC (Twentynine Palms base). Black faults are bounding faults that define the SECSZ (NFTS = North Frontal Thrust System, PMF = Pinto Mountain fault). Other main faults of the SECSZ are: 1 = Helendale, 2 = Lenwood, 3 = Silver Reef, 4 = Old Woman Springs, 5 = Johnson Valley, 6 = Kickapoo, 7 = Homestead Valley, 8 = Emerson, 9 = Camp Rock, 10 = Copper Mountain, 11 = Rodman, 12 = Pisgah, 13 = Lavic Lake, 14 = Bullion, 15 = East Bullion, 16 = Cleghorn Pass, 17 = Cady, 18 = Ludlow, 19 = Sheephole/Cleghorn, 20 = Calumet, 21 = Broadwell Lake, 22 = South Bristol Mountains.
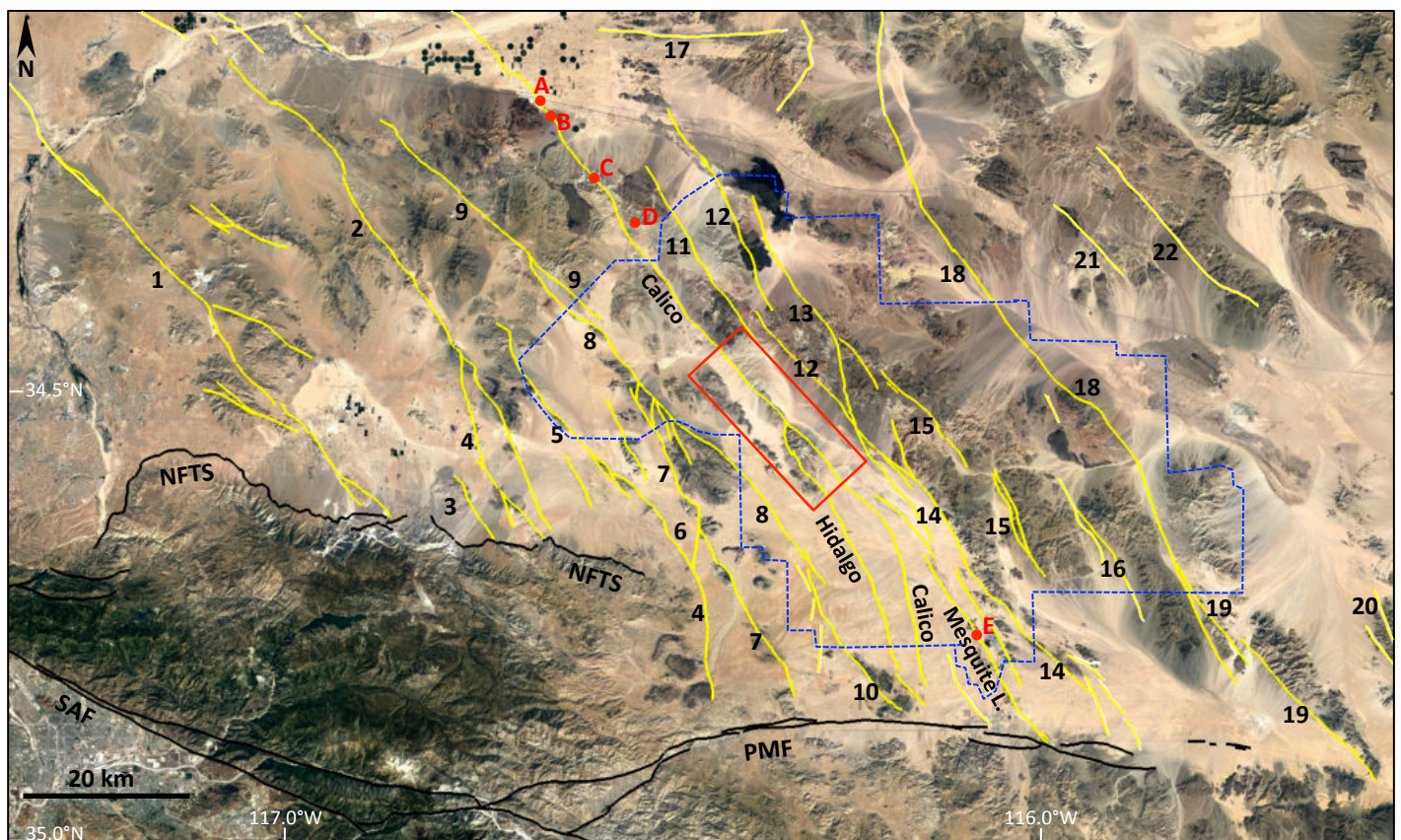
Figure 3: Location map of the study region along the Calico fault system. Interpreted faults are shown in red and Quaternary fold axes in yellow. Box denotes location of Figure 4. Star denotes location of paleoseismic site. CHM = Central Hidalgo Mountain, NHM = North Hidalgo Mountain.
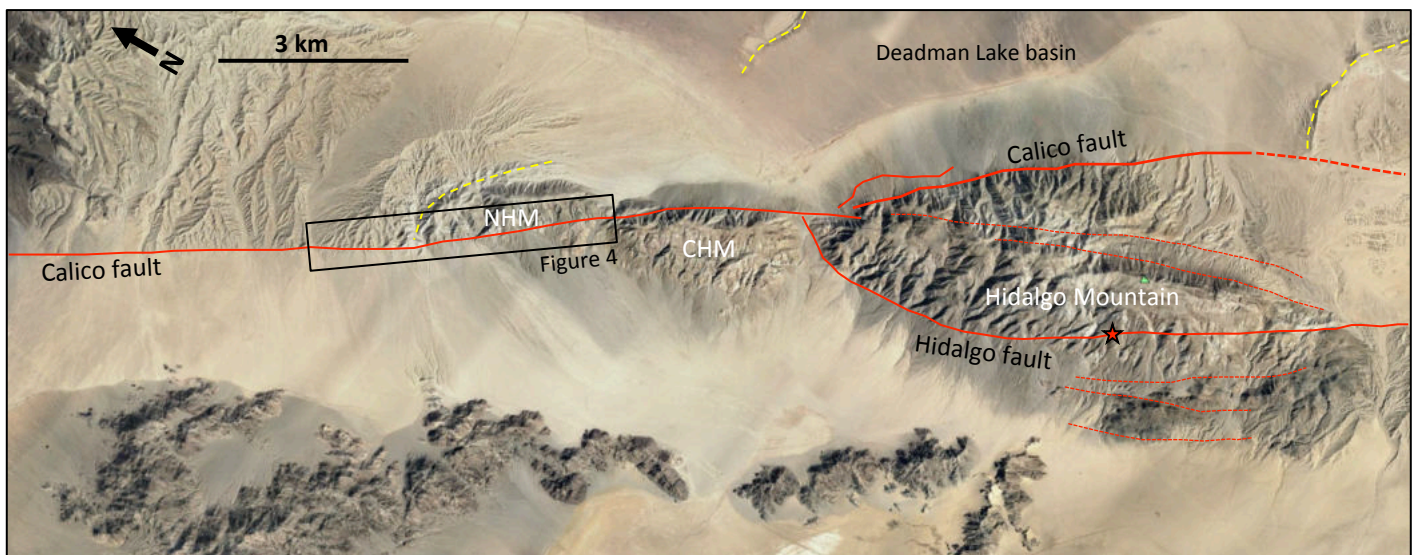
Figure 4: A) Strip map along the Calico fault on North Hidalgo Mountain (location shown in Figure 3). Yellow boxes denote location of shaded relief images in Figures 4b and 4c. Black boxes denote locations of gemorphic maps from Figures 5, 6, and 11. Red line denotes the Calico fault. One OSL age (CF2OSL1=10.7±0.8 ka) and one surface characterization site (S8) are indicated, which do not appear on other maps and which (after further study) do not constrain the age of a reliable offset. B) Shaded relief map from high-resolution topography based on SfM of the northern slip rate area. Location shown in Figure 4a. C) Shaded relief map from high-resolution topography based on SfM of the northern slip rate area. Location shown in Figure 4a. Same scale as Figure 4b.
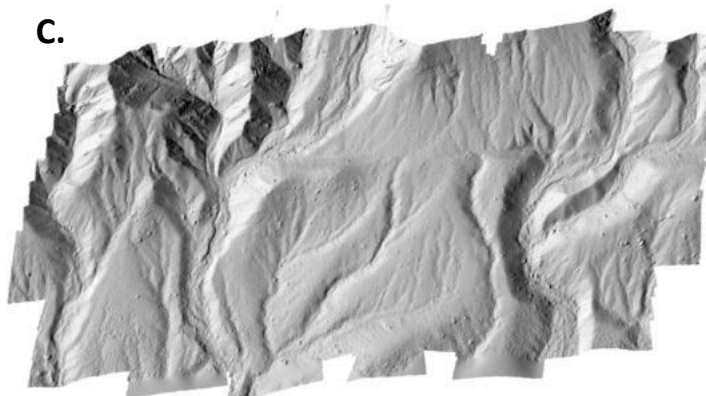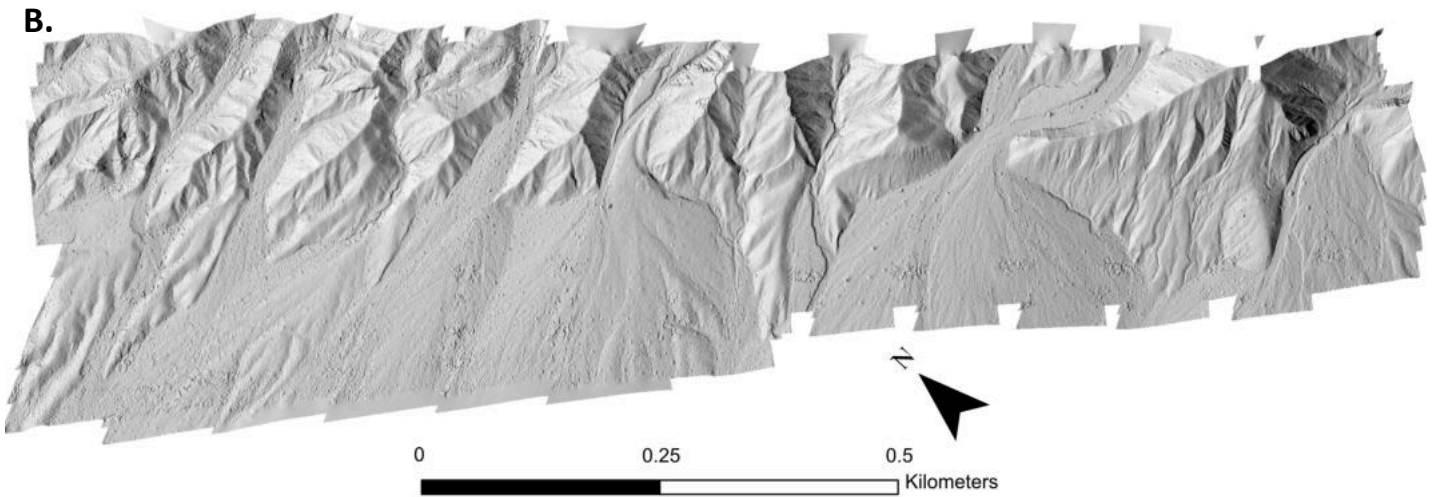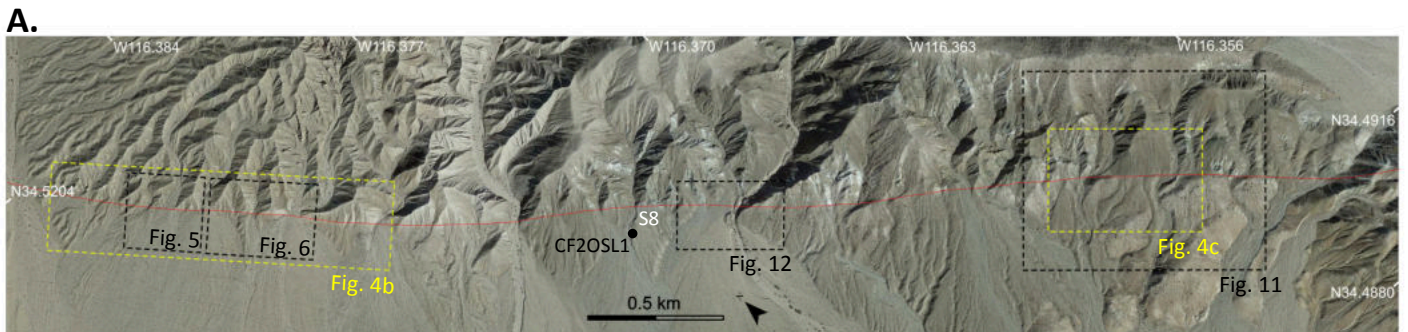
Figure 5: The northernost offset (Offset #1). A) Oblique 3D satellite view of the offset, showing location of surface characterization sites S1 and S1b, the piercing points of the terrace riser and canyon edge, and the location of the OSL sample. Yellow line indicates where riser had to be projected to the fault (missing due to erosion). B) Geomorphic map; see Table 4 for description of geologic units. Riser and canyon edge are shown in blue. C) Reconstruction of 19.2 m offset shown on high resolution topography from SFM. Blue lines point to promontories in the embayed riser that were aligned to define the piercing point. Additional features that align after reconstruction of the offset are shown in red lines.
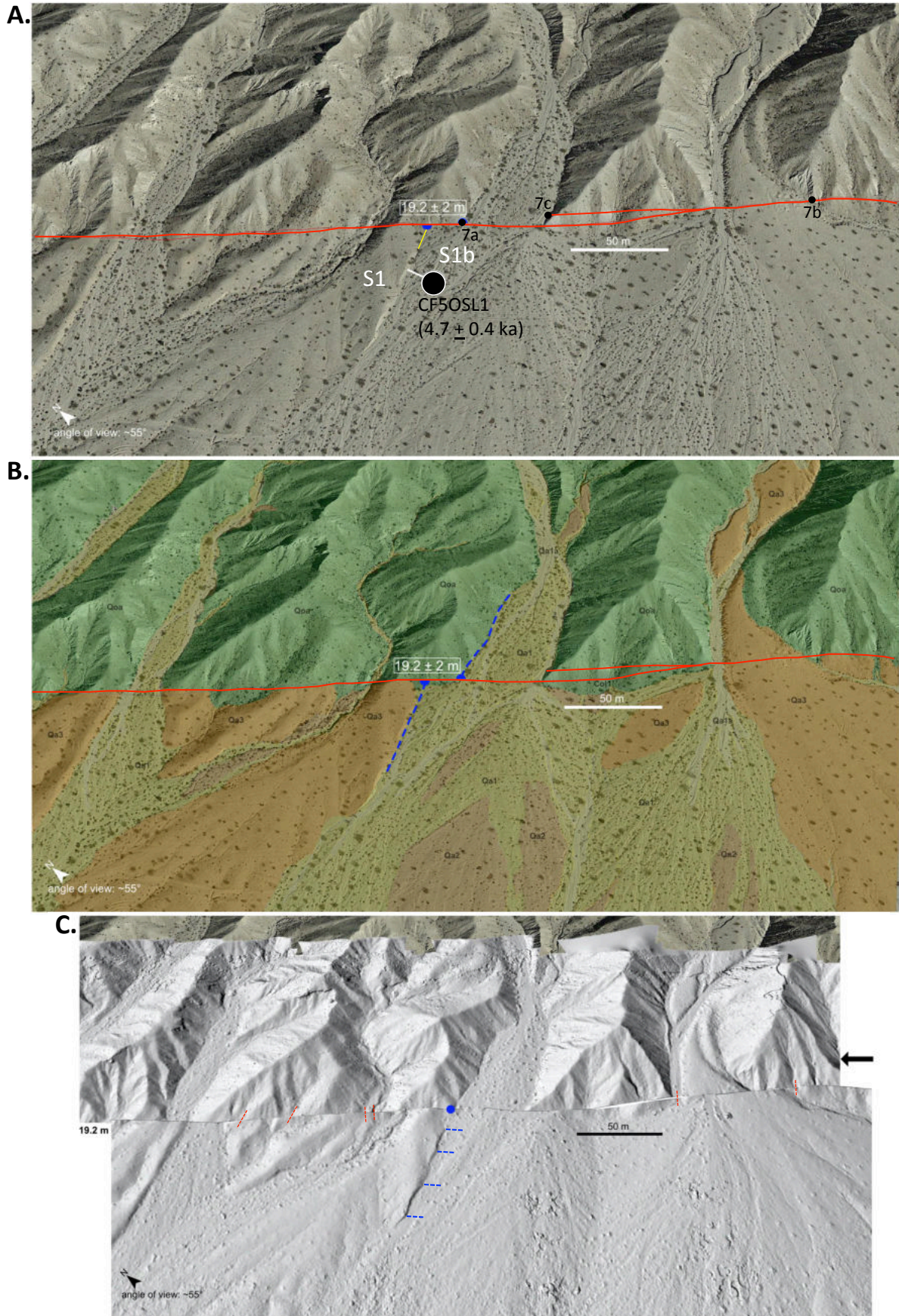
Figure 6: Offset #2 of the northern slip rate area (location shown in Figure 4). A) Oblique 3D satellite view of the offset, showing location of surface characterization site S2 and OSL samples (black circles). Diamond indicates location of CRN depth profile. See text for details of how offset is reconstructed. Fan of S2 site is interepted to restore to Canyon A. Features marked a, b, and c restore to a', b', and c' by the amounts shown. Restoration of b to b' restores the fan riser to the projection of dynamic edge of modern Qa1 wash. B) Reconstruction of 21 m of offset on geomorphic map of the site. See Table 4 for explanation of units. Locations d and e indicate other secondary features that appear to align after restoration of offset.
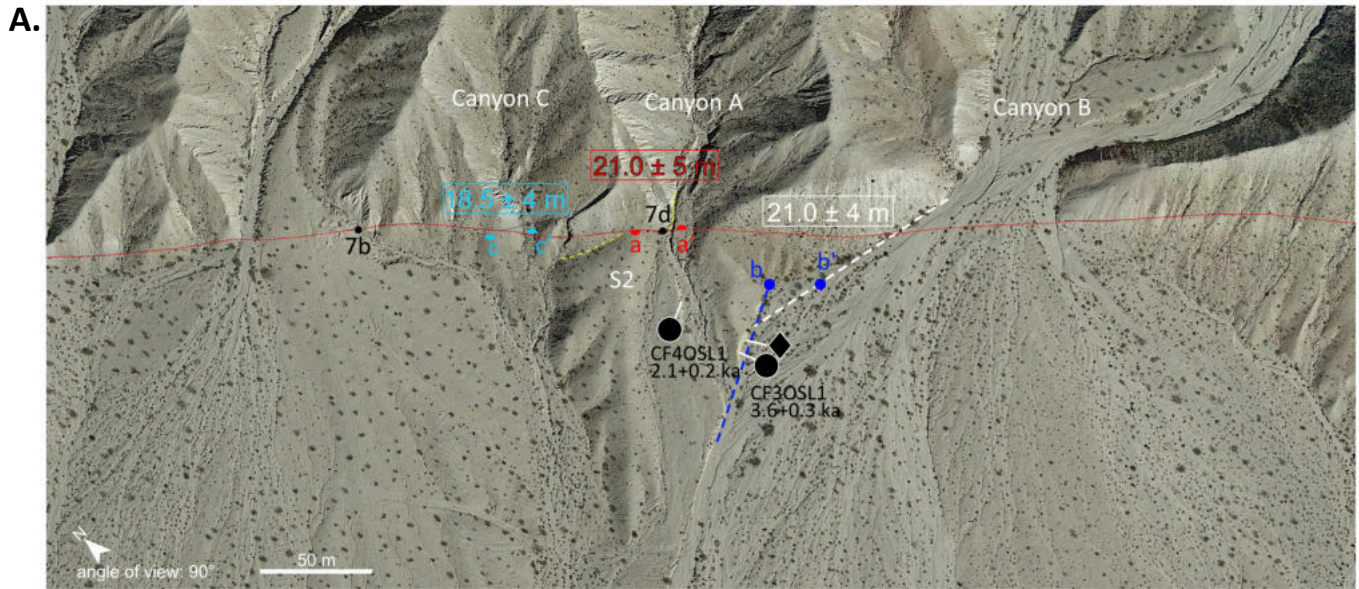
Figure 7: Photographs of fault exposure at select locations. Locations shown in Figures 5 and 6. Figure 7a depicts fault exposure that juxtaposes gouge on the left against older Quaternary alluvium (Qoa) on the right, capped by a younger alluvial deposit (Qa2). Figure 7c depicts dextral offset of fault gouge-cored shutter ridge into a channel (toward the viewer).

Figure 8: Surface characterization sites, including comparison of surfaces (upper left), gravel pavment (upper right), soil pits (lower left), and oxidized base of clasts on the surface (lower right). Locations shown in various figures inidicated by S#. A) Northernmost slip rate area. B) and C) are southern slip area.
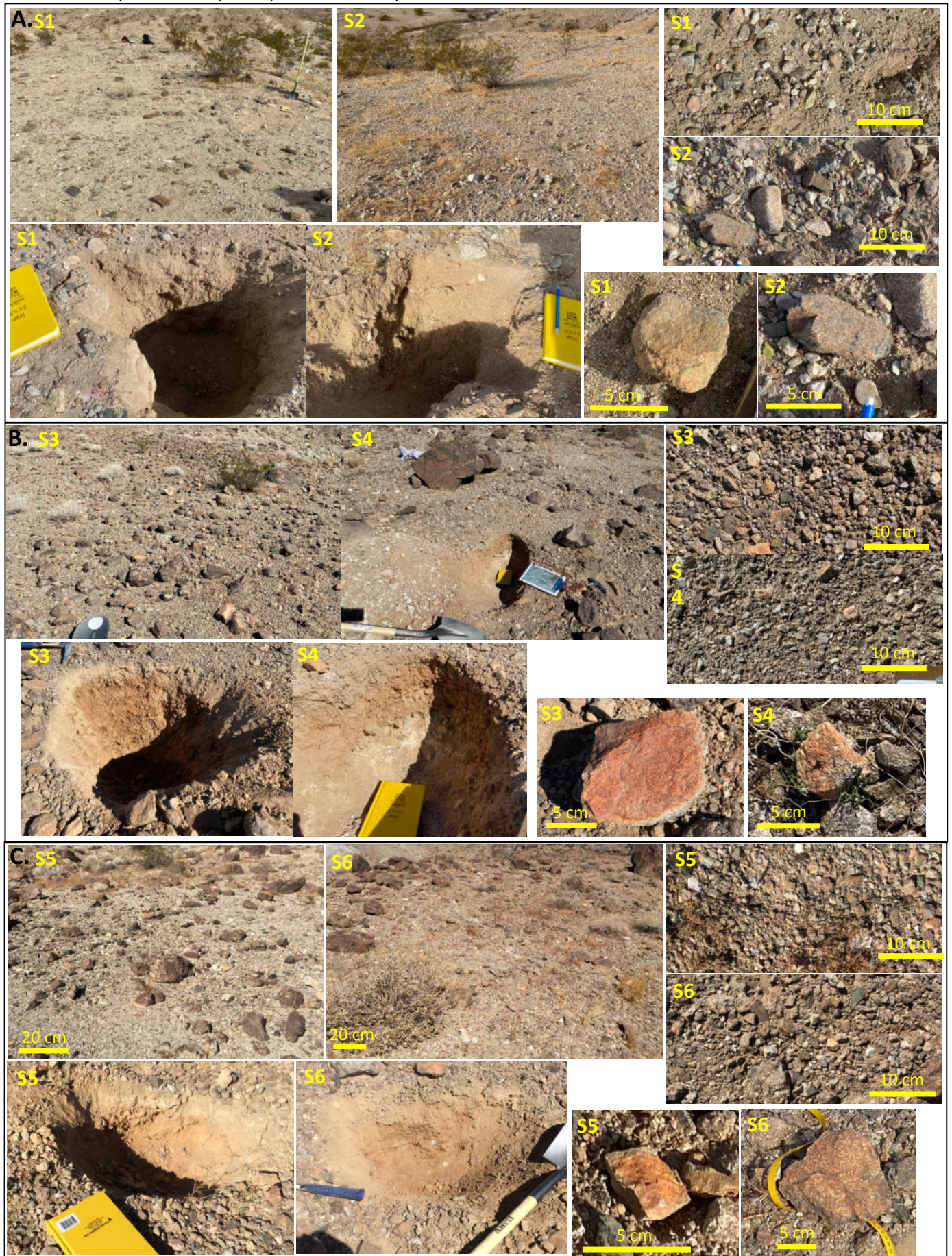
Figure 9: Field photos of Offset #1 in the northren slip rate area (Figure 5). Photo on left is taken from west of the fault and shows the restoration of the terrace riser. Note embayment of the risert at location b. Photo on right is from east of the fault and looks west. Red line denotes approximate reconstruction of the offset of pierce points defined by the riser (a) and the canyon edge to the west (a') of 19.2 m.
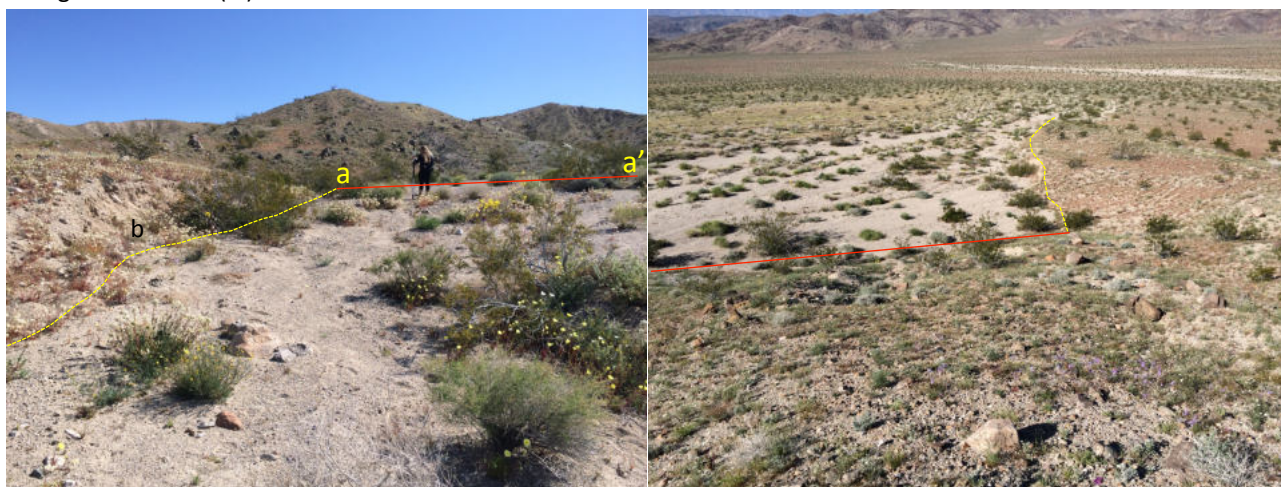
Figure 10: The southern slip rate area. A) Oblique 3D satellite image of the southern slip rate area. Fault is shown in thin black line. Note the obvious disruption and offset of multiple canyons and gullies along the fault trace. B) Oblique Shaded relief image of high-resolution DEM of the southern slip rate area (location shown in Figure 10a and Figure 11). The fault is even more obvious on this image than on the sattlite image. C) Restoration of 52.5 m of offset in the southern slip rate area. This reconstruction aligns numerous canyons and gullies, as well as geomorphic surfaces (shown in Figure 11).
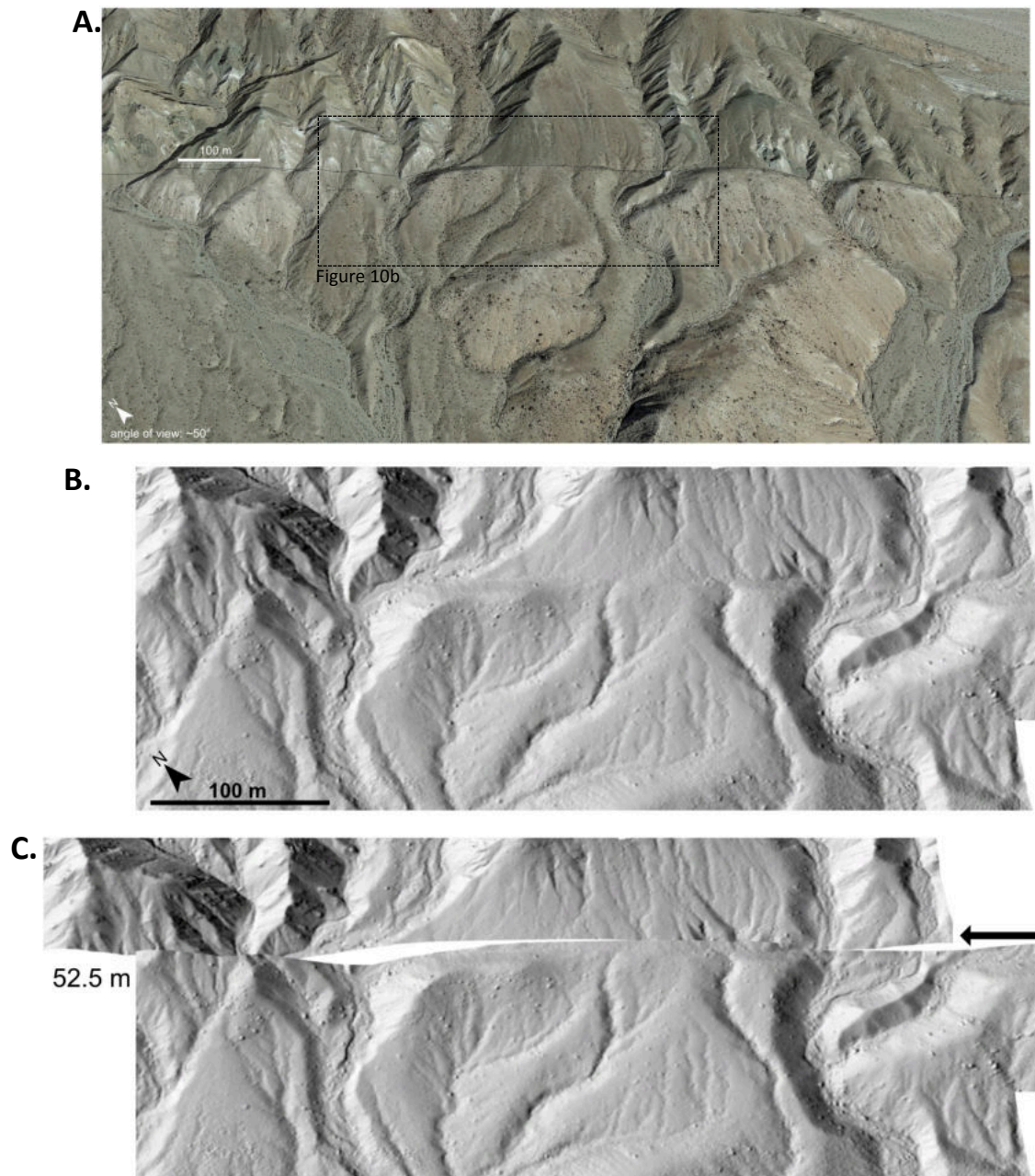
Figure 11: A) Oblique geomorphic map overlain on shaded relief DEM of the southern slip rate area. Unit descriptions are provided in Table 4. See text for description of offsets. Triangles denote locations of boulder TCN ages, whereas boxes denote locations of amalgamated surface quartz samples for exposure ages, none of which are yet available. Three key offsets of canyons are highlighted by dashed lines (59, 52, 49, and 50 m), which average to 52.5 m (the restored offset in Figure 11b). Box denotes location of DEM in Figure 10b. B) Same geomorphic map with 52.5 m dextral offset restored (matches the image in DEM in Figure 10b). Additional offsets that total 100 m (of the center of the Qa6b deposit) and 74 m (of a canyon) are indicated (used for Figure 11c reconstruction). Locations of surface characterization sites S3, S4, and S4b are shown (Figure 8, Table 1).C) Same geomorphic map after 100 m dextral offset restored. This aligns the Qa6b deposit. Locations of surface characterization sites S5, 5b, and 6 shown.
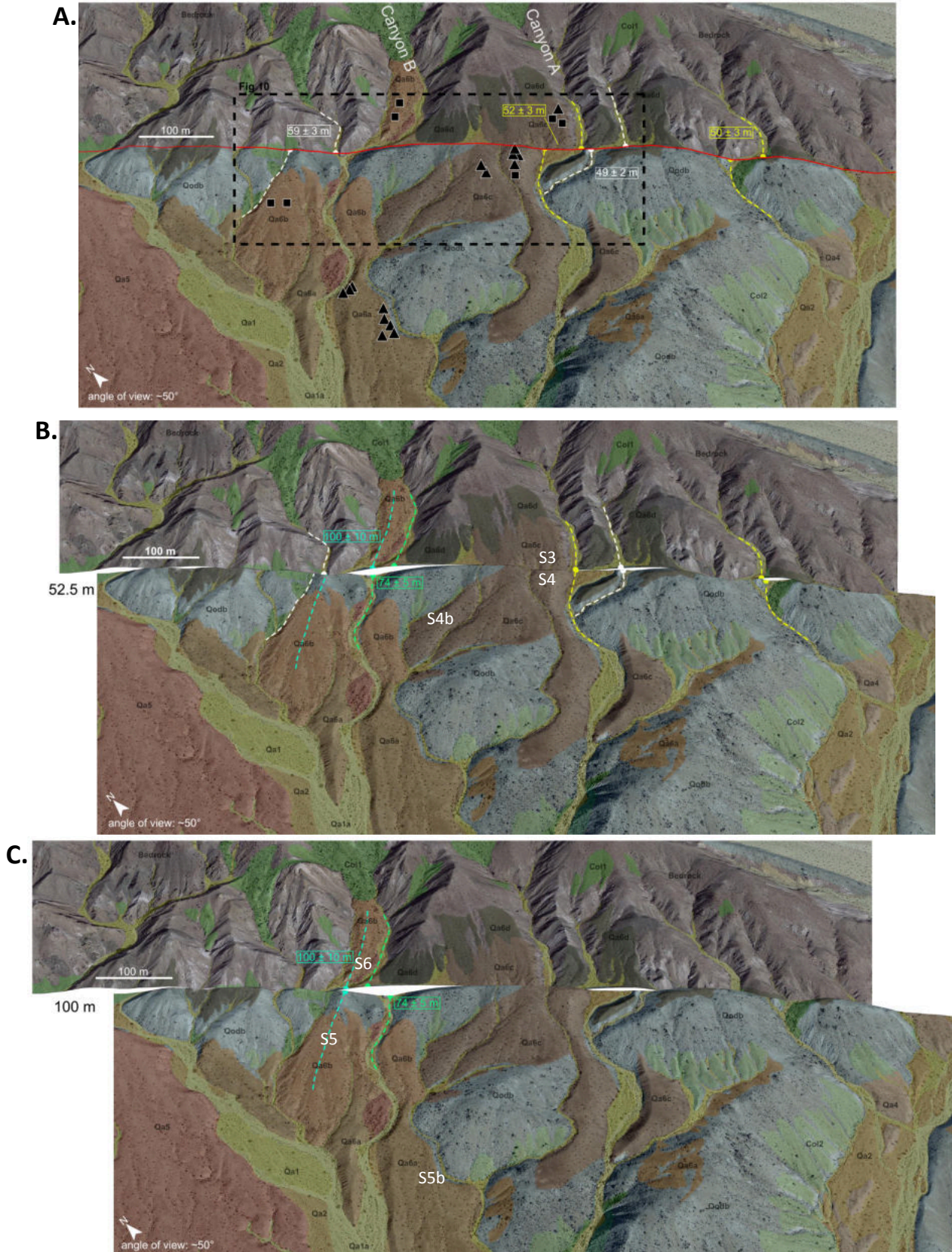
Figure 12: A) Oblique geomorphic map overlain on DEM of the central offset region. See Table 4 for unit descriptions. Yellow dashed line denotes steep canyon margin exposing Qa4 over bedrock, which appears offset ~20 m. The shutter ridge (a) has been offset a greater amount. Post offset, the main drainage incised deeply as an inner gorge (b), with the modern wash now 7 m below Qa4. Prior to capture and rerouting of the canyon, drainage is interpreted to have flowed around the nose of the shutter ridge in the beheaded stream at location c. Location of one new, undated OSL sample shown by black circle (in Qa4 terrace). B) Same geomorphic map after restoration of 20 m right-lateral offset. The canyon margin now aligns (yellow line). The beheaded stream marked as c in Figure 12a now aligns with a gully marked as locaiton d. Location of surface characterization site S7 shown. C) Satellite image of the same offset region (vertical view). White line indicates location of fault for restoration. D) Satellite view after restoration of 20 m pffset, showing how well the canyon edge lines up. The inner gorge at location f would have been incised after the offset, as the ridge moved into the flow of the main drainage, which makes the restoration appear imperfect. E) Photo taken from around S7 looking east at the inner gorge, showing shutter ridge (SR) and the Qa3 and Qa4 terraces. F) Photo taken from just east of the shutter ridge looking east at the inner gorge (IG). G) Photo taken from the Qa4 terrace east of the fault looking west at the shutter ridge and inner gorge. The strip of Qa4 atop bedrock in the view is the short yellow line shown in Figure 12a.
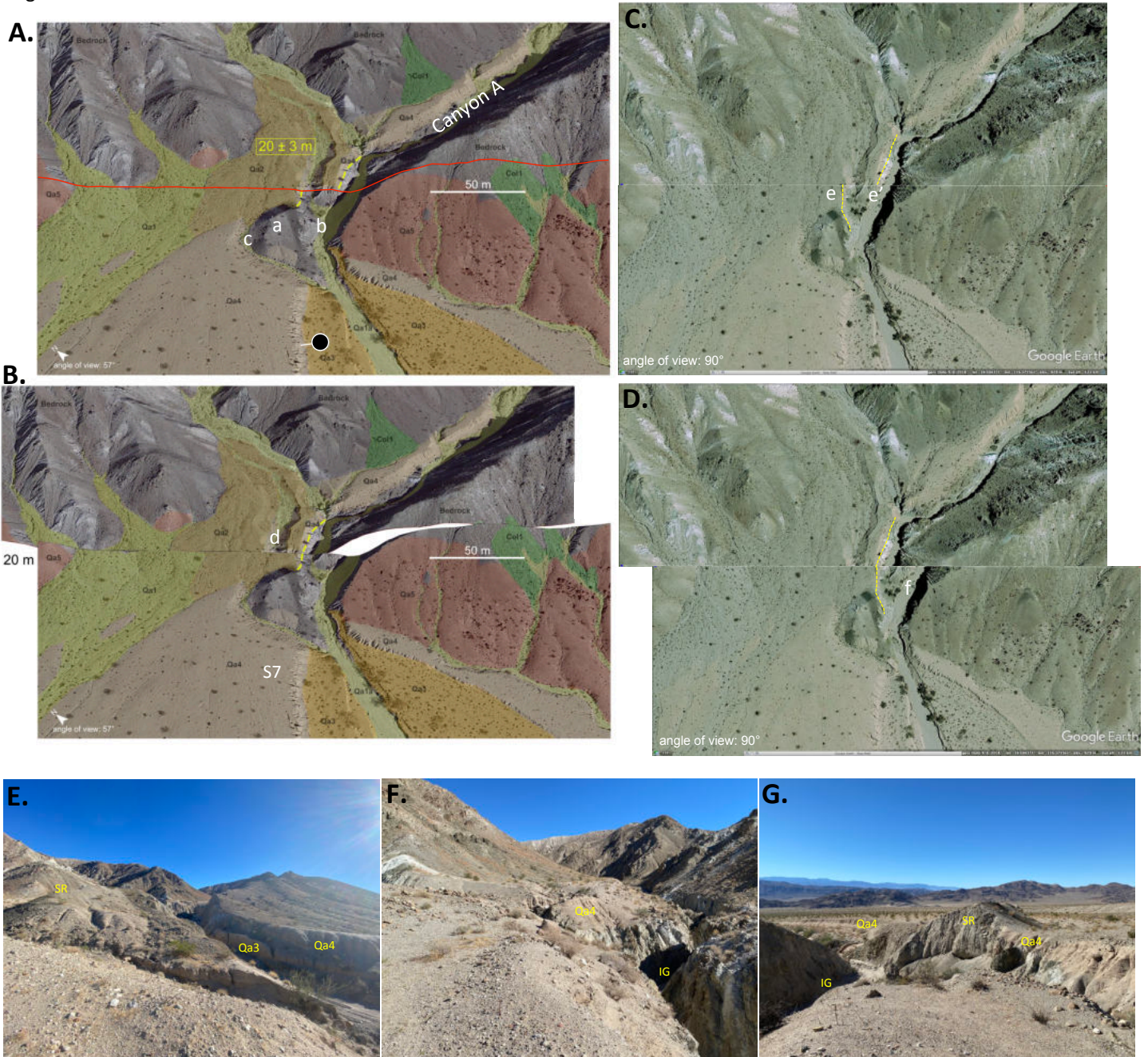
Figure 13: Examples of features used for age constraints in the slip rate study. A) Boulders used for surface exposure TCN dating. B) Depth profile. C) Surface quartz clasts (metasedimentary quartzite on the left, vein quartz on the right). D) OSL site.

Figure 14: Comparison of expression of the paleorupture on satellite imagery with the 1999 Hector Mine surface rupture. Location of paleorupture (top) is 34.45077N, 116.334364W. Location of Hector Mine rupture (bottom) is 34.59686N, 116.29844W.

Figure 15: A) Map of paleorupture of the Hidalgo fault along the west flank of Hidalgo Mountain. Fault traces in dark orange show good evidence in the field for the paleorupture, whereas light orange are sections that were inferred (e.g. connecting between dark orange sections). The paleorupture is lost where crossing the youngest washes, consisting of loose, unconsolidated alluvium, as well as on rugged, debris-covered hisllslopes. The idea terrain for preserving the paleorupture appears to be piedmont surfaces with good pavement. Photograph shows how an exposure below the mapped paleorupture reveals a fault, consisting of two near-vertical shear zones on either side that are ~1 m wide and a central zone of brecciated bedrock. B) Photograph of the paleorupture along the Hidalgo fault (between white lines), from several hundred meters south of the trench site, showing the chararacter of the ground disruption. The paleorupture is defined by a 1-2 m wide path of soft coluvium that appears disarticulated, with loose cobbles and accumulations of fine sediment that appear recently exacavated. The trace is softer than surroundin colluvial surfaces and thus is reminiscent of a deflated mole track. This zone of disruption is linear, continuous, and consistently occurs along the path of deflected gullies and shutter ridges. C) Photo of the paleorupture trace at the trench site, prior to excavation. Note the fine-filled depression bound by two fault strands denoted by white lines. Red box marks the location of excavations.
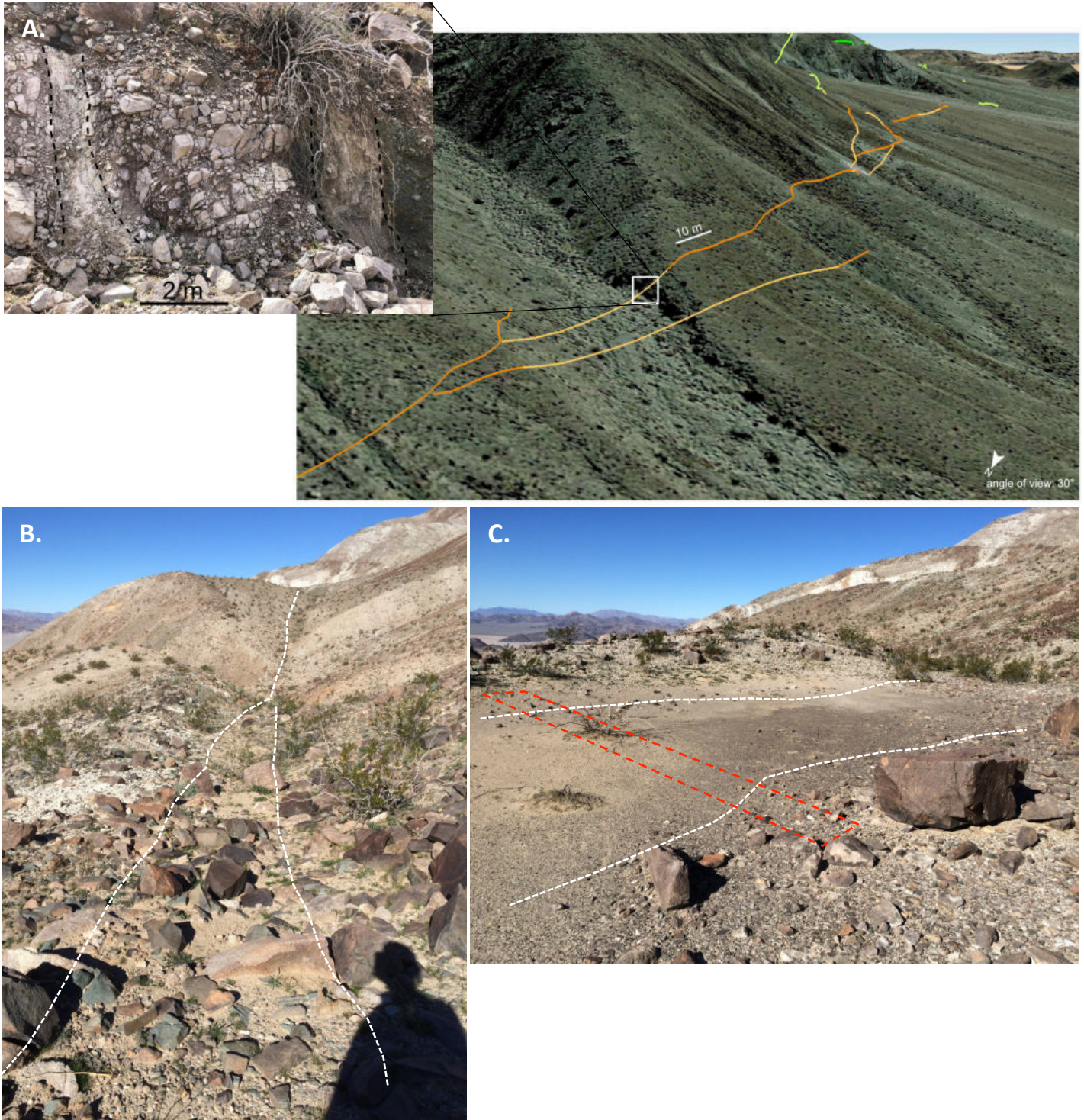
Figure 16: Photographs of the intepreted paleorupture. A-D are pictures of the rupture trace. E-F are pictures of measured offset features. Locations of photos are shown in Figure 17b.
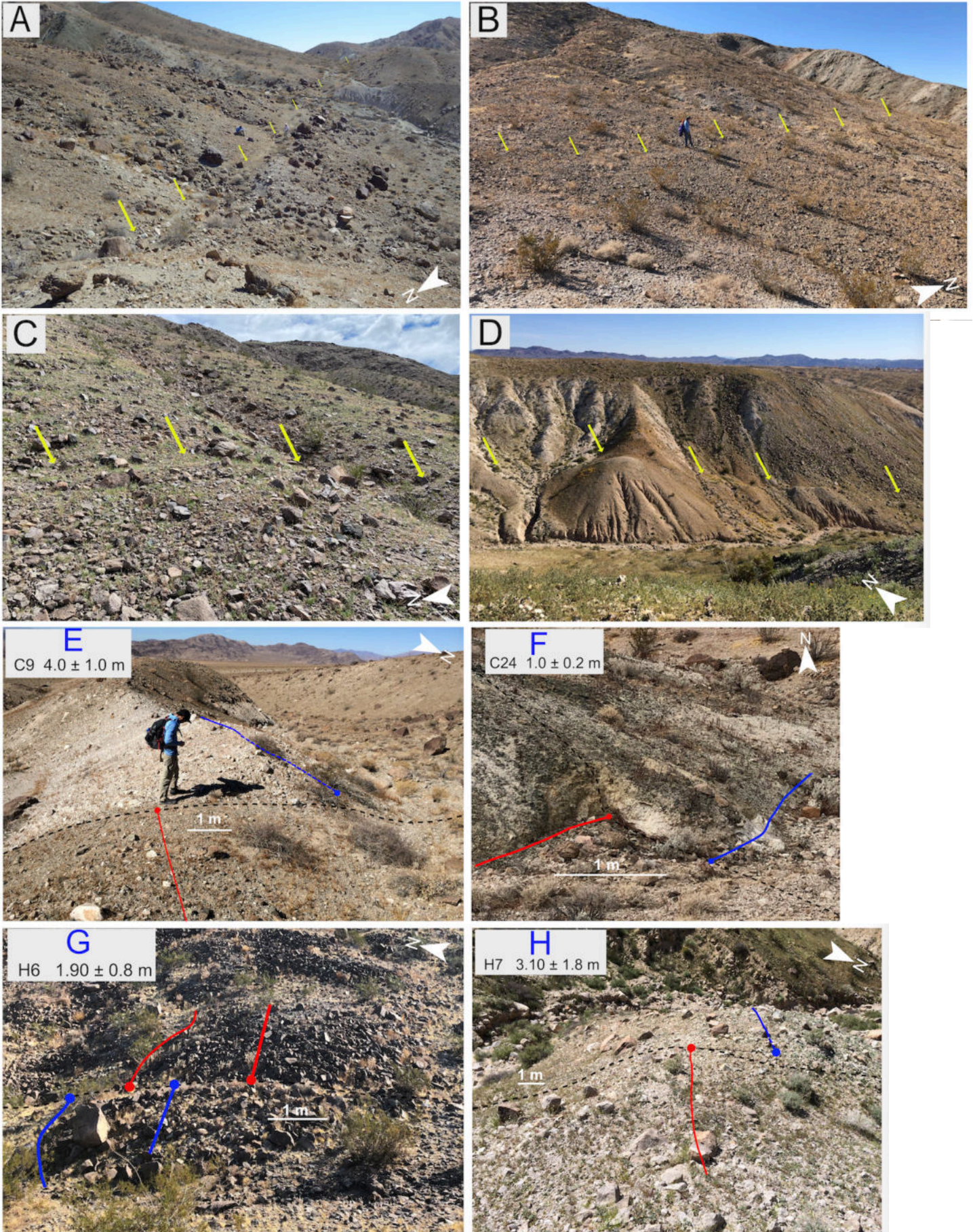
Figure 17: A) Map of the paleorupture. Colors of fault are explained in the legend at base of figure. Orange shades represent field-mapped faults, whereas green shades reprsent faults mapped only via remote imagery. Darker colors indicate where evidence for the paleorupture is stronger. Blue represents potential paleorupture where features are not as well preserved and may represent a separate event. Red star indicates location of the paleoseismic site. Circles and triangles indicate locations of offset measurements (Table 3).B) Map of paleorupture (well-defined trace only, excluding blue lines from Figure 17a) on shaded relief map. This map shows the entire 18 km of surface rupture associated with the event identified in the trench to be 0.7-1.9 ka. Locations A-H show locations of photos in Figure 16.
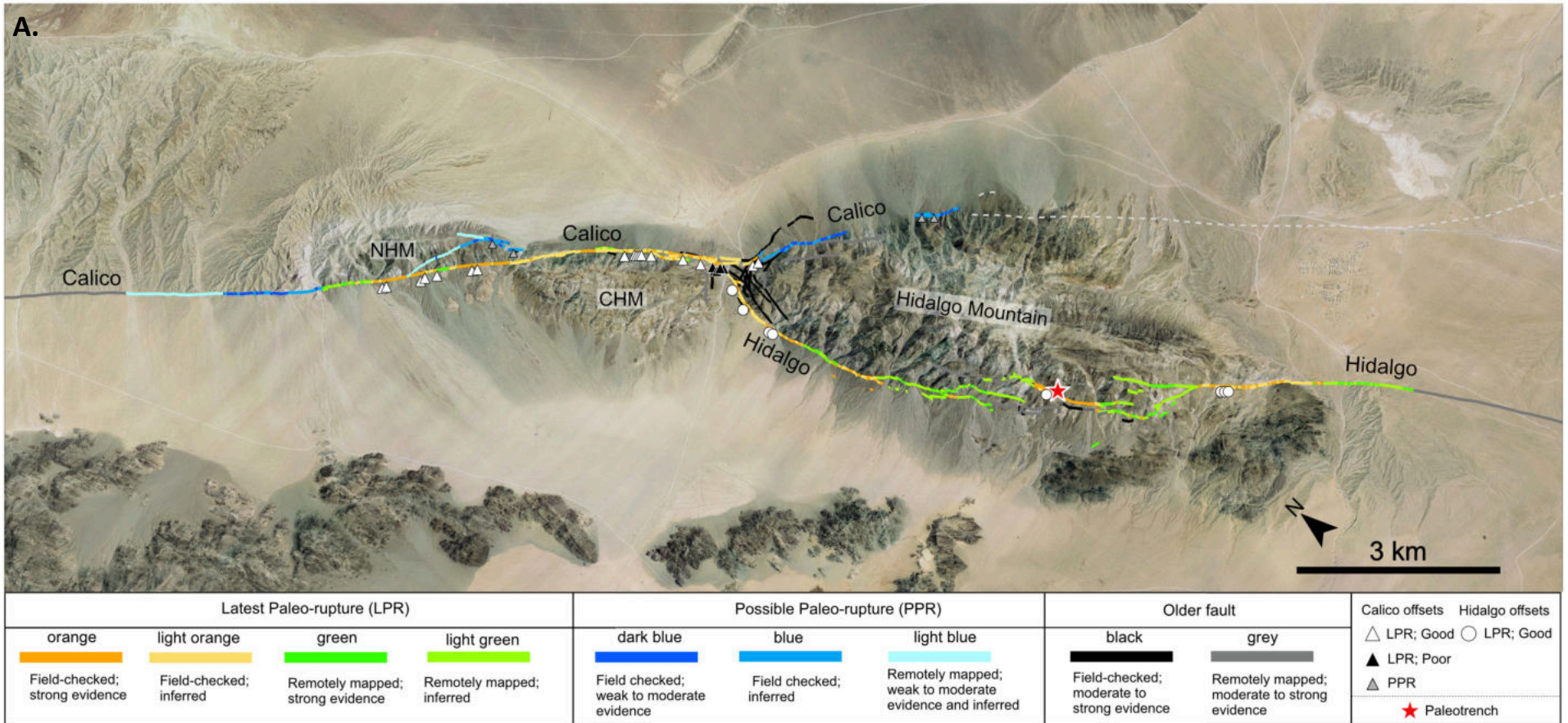
Figure 18: A) Cumulative Offset Probability Distribution (COPD) for offsets along the paleorupture (Table 3). Offsets used exclude those along questionable paleorupture (i.e. blue lines on Figure 17). Although a total of 31 offsets were measured along the main paleorupture, 8 of these were averaged into 1, because they occurred in a small area of the rupture 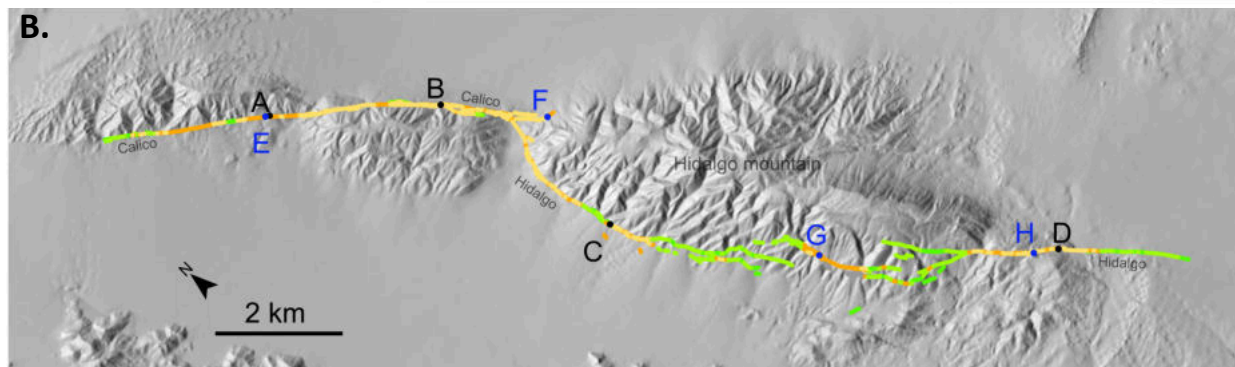where the Hidalgo and Calico faults merge (resulting in n=24 measurements). The largest peak on the COPD is 2.3 m, which we take as the best estimate of average slip during the mapped extent of the paleorupture. Secondary larger peaks may represent multiple events. B) Plot of offset along length of paleorupture from north to south. Symbols indicate which fault and the quality of the offset measurement. The plot shows n=28 measurements, which excludes 4 of the original 35 that occur along questionable rupture traces (i.e. blue lines) and 3 that are greater than 6 m, which we infer to be due to multiple events. Yellow shaded area indicates region of many overlapping offsets where the Calico and Hidalgo faults merge, which were combined into a single average offset for construction of the COPD in Figure 18a. Red line shows the running average at 1-km spacing, which assumes a linear trend in offset change along rupture segments without offset measurements (where offset is inferred from neighboring segments).
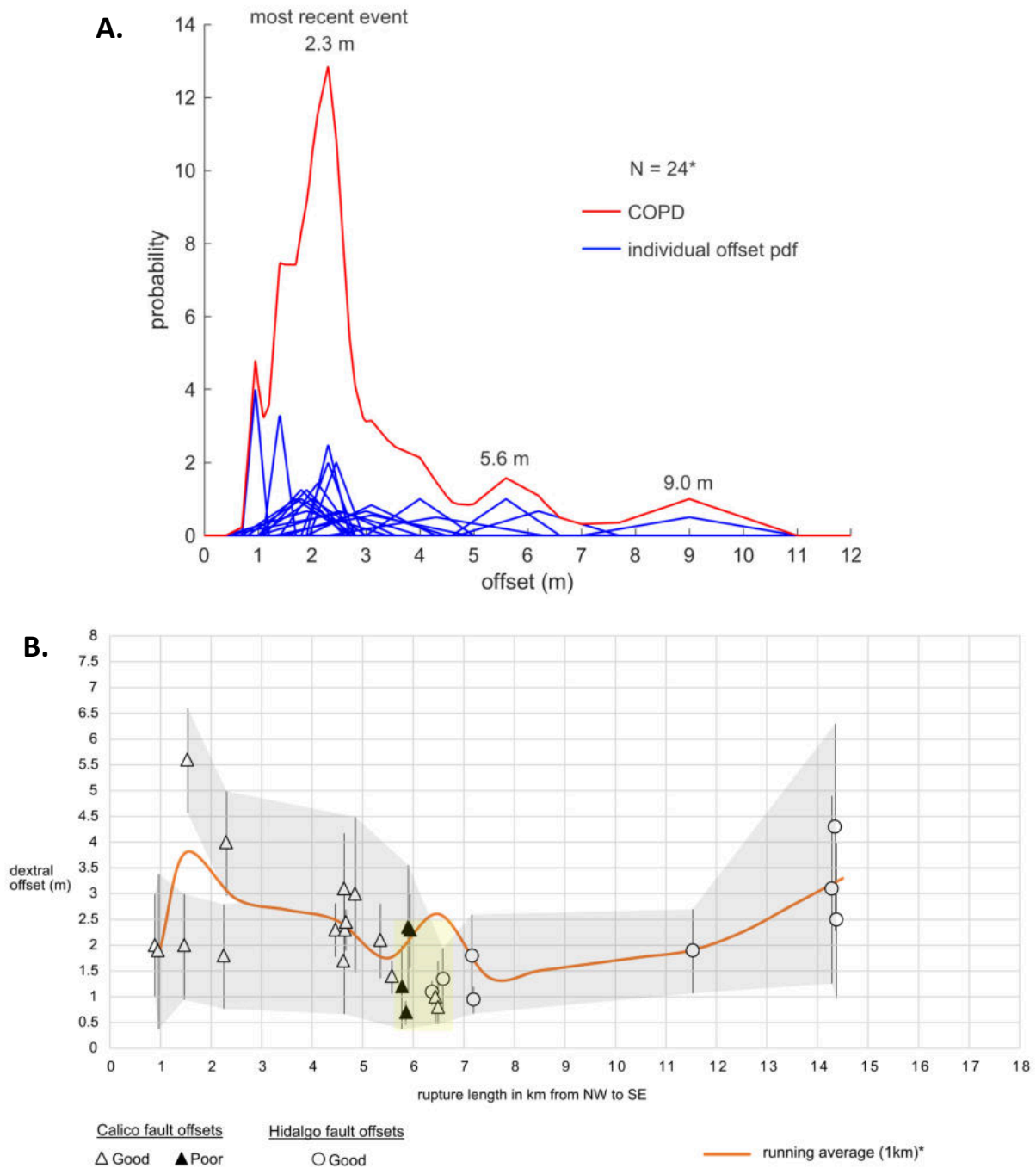
Figure 19: Results from paleoseismic trench across the Hidalgo fault paleorupture. A) SfM derived shaded relief map of the trench location, showing T1 and T2. Location of this figure is denoted by the red star on Figure 17a. Red lines indicate mapped faults inferred to be paleorupture. Photo of site is given in Figure 15c. B) Photomosaic and interpretation of trench T1 (south wall). Location of OSL samples and resulting age (ka, BP) (Table 2). C) Photomosaic and interpretation of trench T2 (south wall). The larger mosaic shows the full length of the trench, whereas the expanded image shows the detail of the western end.

Table 1: Characteristics of alluvial surfaces used in offset reconstruction.

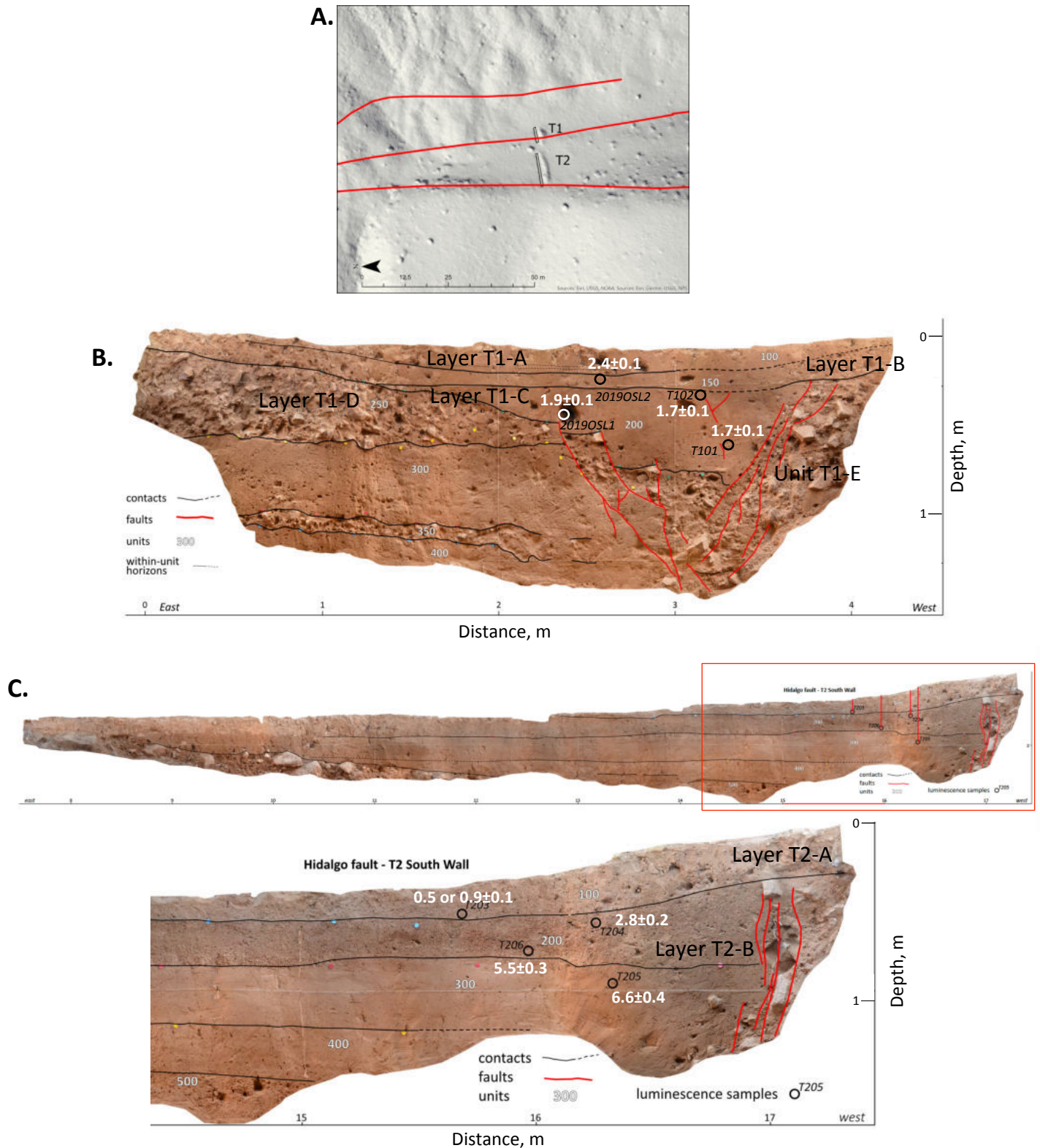| Site	% Weathered (1)	Color of BT Horizon (2)	Basal Clast Oxidation (3)	Gravel Pavement (4)	Varnish on Non-Granitic Clasts	Soil Hardness	Pedogenic Carbonate	% Clasts >10 cm (5)	Max. clast size (cm) (6)	Clast Shape	Recycled Clasts (7)	Clast composition (8)
S1	13.4	10YR6/3	patchy, pale orange	0.3 cm, weak	light (brown) on some	very soft	none	2.5	25-50	rounded/ semi-rounded	yes, many	PM, Lg, QC, Ep, FG, II, Gr, G/B
S1b	0	-	-	-	-	-	-	2.4	25-50	rounded/ semi-rounded	yes, many	Gr, Lg, QC, PM, VB, FG, G/B, Ry, II
S2	12.9	10YR6/3	patchy, pale orange	none	none	very soft	none	0.8	25	rounded/ semi-rounded	yes, many	PM, Gr, FG, Lg, QC, VB, II, Ry
S3	42.0	5YR5/6 to 2.5YR5/6	dark red, extensive	2 cm, well defined	medium (brown)	very hard	minor	5.1	50-100	semi-angular	no	**PM**, G/B, Lg, QV, Gr, FG
S4	42.7	5YR5/6 to 2.5YR5/6	reddish orange, complete except where eroded	2 cm, well defined	medium (brown)	very hard	strong	16.3	>100	semi-angular	no	**PM**, Lg, G/B, QV, FG
S4b	43.4	7.5YR4/6 (wet)	reddish orange, complete	1-2 cm,well defined	light (brown)	medium to soft	none	12.3	>100	semi-angular	no	**PM**, Lg, G/B, Db
S5	41.9	7.5YR5/6 to 5YR5/6 (wet)	reddish orange, complete	1-2 cm, well defined	medium (brown)	hard	none	7.6	>100	semi-angular	no	**PM**, Lg, G/B
S5b	42.4	10YR5/6 to 7.5YR5/6 (wet)	reddish orange, complete	1-2 cm, well defined	medium (brown)	medium	none	23.1	>100	semi-angular	no	**PM**, Lg, G/B
S6	23.9	7.5YR5/6 (wet)	reddish orange, complete	2 cm, well defined	medium (brown)	hard	none	12	>100	semi-angular	no	**PM**, Lg, Db, G/B,
S7	18.8	10YR6/3	patchy, pale pink on quartzite only	1 cm, moderate	none	medium to soft	none	0.5	25	semi-rounded	yes	**PM**, QC, Lg, G/B, Ry, FG
S8	45.5	10YR6/4	pale orange, complete in center	2-3 cm, well defined	light (brown) on some	medium	none	2.9	25-50	semi-angular	no	**PM**, Lg, Gr, QV, FG, G/B

1) Of 10-25 cm diameter clasts

2) Maximum color, usually at 20 cm depth

3) Of surface clasts

4) Surface lag gravel

5) By volume, clasts >10 cm diameter, median axis

6) Median axis

7) Clasts recycled from Qoa

8) Of clasts >10 cm, in order of concentration; boldface indicates >50% of clasts: PM = porphyritic monzonite, Lg = leucogranite,

G/B = greenstone/altered basalt, Db = diabase (non-vesicular basalt), QV = vein quartz, Gr = granite, FG = fine granite

QC = metasedimentary quartzite cobble, Ep = epidote vein, VB = vesicular basalt, Ry = rhyolite, II = intermediate intrusive

Table 2: Summary of luminescence dating results for samples from extracted from sediment, sample locations, radioisotopes concentrations, moisture contents, total dose-rates, D_E estimates and optical ages. **Preferred ages are shown in bold**.

Sample number	Location (°N/°W)	Altitude (m asl)	Depth (cm)	U[a] (ppm)	Th[a] (ppm)	K[a] (%)	Rb[a] (ppm)	Cosmic[b,c] (Gy/ka)	Dose-rate[b,c,d] (Gy/ka)	n[e]	Average equivalent dose[f] (Gy)	Weighted average equivalent dose[h] (Gy)	2-mixed model equivalent dose[i] (Gy)	Average OSL/IRSL Age[f,j] (ka)	Weighted average OSL/IRSL Age[h,j] (ka)	2-mixing model OSL/IRSL Age[h,i,j] (ka)
CF2OSL1	34.5056/ 116.3755	927	115	4.8	40.8	2.30	88.9	0.22±0.02	7.49±0.54	27(27) [38%]	113.2±6.4	90.4±2.1	79.9±2.6 (27%)	15.1±1.4	12.1±0.9	**10.7±0.8**
CF3OSL1	34.5144/ 116.3848	935	130	3.7	28.8	3.00	110	0.21±0.02	5.50±0.33	26(30) [38%]	41.6±4.1	33.5±0.5	19.9±0.9 (51%)	7.6±0.9	6.1±0.4	**3.6±0.3**
CF4OSL1	34.5147/ 116.3849	936	55	3.6	20.1	3.20	123	0.23±0.02	5.16±0.32	38(52) [43%]	28.5±4.0	11.9±0.4	10.7±0.5 (71%)	5.5±0.9	2.3±0.2	**2.1±0.2**
CF5OSL1	34.5172/ 116.3873	932	46	4.0	26.7	3.20	114	0.23±0.02	5.66±0.34	25(28) [20%]	46.3±3.3	34.1±1.1	26.5±1.6 (27%)	8.2±0.8	6.0±0.4	**4.7±0.4**
2019HFOSL1	34.4265/ 116.3158	1000	44	3.4	21.0	2.10	106	0.24±0.02	4.19±0.24	23(26) [20%]	5.4±0.3	5.0±0.1	- (20%)	**1.3±0.1**	1.2±0.1	**n/a**
2019HFOSL1	34.4265/ 116.3158	1000	44	3.4	21.0	2.10	106	0.24±0.02	5.29±0.34	28(30) [n/a]	10.1±0.2	9.9±0.1	- (10%)	**1.9±0.1**	1.9±0.1	**n/a**
2019HFOSL2	34.4265/ 116.3158	1000	16	3.2	21.3	2.20	106	0.25±0.02	4.30±0.25	30(31) [64%]	13.0±1.0	11.4±0.2	10.2±0.3 (30%)	3.0±0.3	2.6±0.2	**2.4±0.2**
HFT101	34.4265/ 116.3158	1000	60	3.3	21.5	2.20	124	0.23±0.02	5.37±0.35	31(47) [97%]	10.1±0.6	9.3±0.1	9.35±0.13 (21%)	1.9±0.2	1.7±0.1	**1.7±0.1**
HFT102	34.4265/ 116.3158	1000	25	3.6	22.2	2.10	106	0.24±0.02	5.47±0.36	42(54) [93%]	10.4±0.5	9.4±0.1	9.5±0.1 (23%)	1.9±0.2	1.7±0.1	**1.7±0.1**
HFT203	34.4265/ 116.3160	1000	12	4.0	27.1	2.20	96.1	0.25±0.02	4.84±0.28	32(39) [25%]	7.5±1.2	2.9±0.1	2.4±0.1 (71%)	1.5±0.3	0.6±0.1	**0.5±0.1**
HFT203	34.4265/ 116.3160	1000	12	4.0	27.1	2.20	96.1	0.25±0.02	6.11±0.40	31(31) [n/a]	5.8±0.2	5.7±0.1	- (13%)	**0.9±0.1**	0.9±0.1	**n/a**
HFT204	34.4265/ 116.3160	1000	25	3.9	26.9	2.00	103	0.24±0.02	4.59±0.26	25(26) [59%]	17.6±1.3	14.1±0.2	13.1±0.3 (32%)	3.8±0.4	3.1±0.2	**2.8±0.2**
HFT205	34.4265/ 116.3160	1000	54	3.2	23.9	2.00	105	0.24±0.02	4.23±0.25	29(32) [56%]	34.9±1.8	31.0±0.5	27.8±0.7 (25%)	8.3±0.6	7.3±0.5	**6.6±0.4**
HFT206	34.4265/ 116.3160	1000	32	4.3	31.4	2.00	102	0.24±0.02	4.95±0.28	25(26) [92%]	31.8±3.7	24.9±0.5	27.0±0.5 (36%)	6.4±0.8	5.0±0.3	**5.5±0.3**

[a] Elemental concentrations from ICP-MS of whole sediment measured at Activation Laboratories Limited Ancaster, Ontario Canada.

[b] Estimated fractional day water content for whole sediment is taken as 10% and with an uncertainty of ± 5%.

[c] Estimated contribution to dose-rate from cosmic rays calculated according to Prescott and Hutton (1994). Uncertainty taken as ±10%.

[d] Total dose-rate from beta, gamma and cosmic components. Beta attenuation factors for U, Th and K compositions incorporating grain size factors from Mejdahl (1979). Beta attenuation factor for Rb is taken as 0.75 (cf. Adamiec and Aitken, 1998). Factors utilized to convert elemental concentrations to beta and gamma dose-rates from Adamiec and Aitken (1998) and beta and gamma components attenuated for moisture content. Dose rates calculation was confirmed using the Dose Rate and Age Calculator (DRAC) of Duncan et al. (2015).

[e] Number of replicated equivalent dose (D_E) estimates used to calculate D_E. These are based on recuperation error of < 10%. The number in the parentheses is the total measurements made including failed runs with unusable data. The number in square parentheses is the percentage of aliquots that were used in 2 mixing model.

[f] Average equivalent dose (D_E) determined from replicated single-aliquot regenerative-dose (SAR; Murray and Wintle, 2000) runs. The uncertainty is the standard error and includes an uncertainty from beta source estimated of ±2.5%.

[h] Weighted average equivalent dose (D_E) determined from replicated single-aliquot regenerative-dose (SAR; Murray and Wintle, 2000) runs. The uncertainty is the standard error and includes an uncertainty from beta source estimated of ±2.5%.

[i] Age based on minimum population in 2-mixing model using the program of Vermeesch (2009). Values in parentheses are the dispersion of the aliquots.

[j] Uncertainty incorporate all random and systematic errors, including dose rates errors and uncertainty for the D_E.

Table 3: Offsets measured along the paleo-rupture (Figures 17, 18).

North to South	offset (m)	error (± m)	feature	Lat	Lon	# of events
C1	2	1	shutter	34.503480	-116.370460	1
C2	1.9	1.5	channels	34.503070	-116.369975	1
C3^	9	2	shutter	34.502110	-116.368650	>1?
C4	2	1	shutter	34.500150	-116.365540	1
C5	5.6	1	alluvial fan	34.499740	116.365060	≥1?
C6^	9	2	channel	34.499038	-116.363732	>1?
C7	1.8	1	channel	34.495618	-116.359168	1
C8^	6.2	1.5	channel	34.495618	-116.359168	>1?
C9	4	1	spur ridge	34.495289	-116.358767	1
C10*	4	1.25	spur ridge	34.495766	-116.354174	1
C11*	2.8	0.5	channel	34.493099	-116.353441	1
C12	2.3	0.5	shutter	34.481650	-116.342152	1
C13	1.7	1	shutter	34.480626	-116.340973	1
C14	3.1	1.2	shutter	34.480497	-116.340908	1
C15	2.3	0.4	levee	34.480401	-116.340817	1
C16	2.45	0.5	spur ridge	34.480183	-116.340681	1
C17	3	1.5	shutter, channel	34.478925	-116.339438	1
C18	2.1	0.7	shutter	34.475194	-116.336493	1
C19	1.4	0.3	channel	34.473459	-116.335263	1
C20"	1.2	0.8	channel	34.471918	-116.334293	1
C21"	0.7	0.2	channel	34.471143	-116.334161	1
C22"	2.35	1.2	channel	34.470881	-116.333853	1
C23"	2.3	0.7	channel	34.470603	-116.333611	1
C24	1	0.2	channel	34.467588	-116.329607	1
C25	0.8	0.3	shutter	34.467497	-116.329229	1
C26*	1	0.3	shutter	34.454648	-116.307381	1
C27*	0.7	0.2	channel	34.454648	-116.307381	1
H2	1.1	0.6	channel	34.466839	-116.335011	1
H3	1.35	0.6	channel	34.464932	-116.335994	1
H4	1.8	0.8	shutter	34.459871	-116.336370	1
H5	0.95	0.25	channel	34.459657	-116.336336	1
H6	1.9	0.8	boulder lobe	34.426717	-116.315811	1
H7	3.1	1.8	shutter	34.409262	-116.297213	1
H8	4.3	2	shutter	34.409260	-116.297200	1
H9	2.5	1.5	shutter	34.409020	-116.296990	1

^ - not included in slip distribution graph (possibly multiple events)
* - not included in slip distribution or COPD (occurs on uncertain trace; marked blue in Figure 17)
" – included in COPD and slip distribution, but low level of confidence in accuracy

Table 4: Description of units shown in geomorphic maps (Figures 5, 6, and 11).

Qa1a – Youngest, most active channel and wash. Interpreted deposition and reworking semi-annually. Broad, sandy channel with little microtopography, due to continuous erosional washouts during precipitation events. Appears as a bright beige or light gray color in satellite imagery.

Qa1 – Active alluvium. Deposition and erosion expected on decadal to centennial timescale from storm events. Bajada-like, with bar and swale topography. Appears as a ribbed or anastomosing bright beige or light gray color in satellite imagery.

Qa2 – Youngest inactive alluvium to rarely active alluvium. Generally inferred to be inactive, except in the largest millennial precipitation events. Commonly terraced 0.5-1 m above active channels. Exhibits reduced bar and swale topography and sandy matrix with no pavement development. Appears as a light brown or gray surface on satellite imagery.

Qa3 – Older, inactive alluvium. Based on soil development and existing age constraints, generally on the order of several thousand years old. Typically forms treads that are 1-3 m above active washes. Exhibts flattened depositional surfaces with poor pavement development. Appears as light brown or gray elevated surface on satellite imagery.

Qa4 – Inactive alluvium (older than Qa3). Expected to be 10-20 ka in age. Typically forms treads that are incised 3-5 m above active wash. Exhibits flat depositional surfaces with moderate pavement development. Appears as light brown or gray elevated surface on satellite imagery.

Qa5 – Inactive alluvium (older than Qa4). Unknown age. Typically forms treads that are incised 3-5 m above active wash. Exhibits better pavement and older characteristics than Qa4. Appears as a brown elevated surface on satellite imagery.

Qa6 – Oldest inactive piedmont alluvium (older than Qa5). Unknown age. Typically forms treads that are incised 4-8 m above active washes. Exhibits flat depositional surfaces with good to well-developed desert pavement and numerous indicators of old age. Appears as dark brown surfaces on satellite imagery. Subscripts denote separate distinctive fan and canyon source, some of which vary in provenance (units may or may not be age-correlative): a = sourced from Canyon B (Figure 11a) b = unknown source, c = sourced from slope between Canyon A and B and Canyon A, d = mafic bedrock source from higher elevations and ridge south of Canyon A.

Qoa - Old Quaternary (inferred) alluvium that predates uplift of North Hidalgo Mountain. This unit forms the plunging anticline that is deposited over Qodb and bedrock. Conists of NE to NW dipping fanglomerate beds with extensive sand-dominated intervals. Contains a wide variety of well-rounded, larges clasts, including metasedimentary quartzite, vesicular basalt, and pink rhyolites of presumed origin in the Bullion Mountains.

Qodb – Old Quaternary (inferred) boulder-rich debris. Consists of a single interval (>5 m thick) of poorly sorted, matrix-supported debris that contains rounded to semi-rounded cobbles and boulders as larges as 2 m diameter. Matrix is sandy and angular. Boulders are typically porphyritic monzonite with large feldspar crystals, with minor leucogranite and orange quartzite. Many clasts appear weathered prior to deposition. Unit is inferred to be a single-event mega debris flow sourced from an unknown location. Is deposited atop bedrock that (where exposed) exhibits an extremely well developed saprolite.

Col1 – Active colluvium. Found on steep ridge slopes as talus aprons above and on active drainages.

Col2 –Colluvium derived solely from Qodb. Is rich in recycled orange oxidized quartzite clasts on surface. Exhibits distinct smooth, light orange appearance on satellite image that mimics an old alluvial pavement.

S – Saprolite.

Bedrock – Consists of porphyritic monzonite, granite, leucogranite, mafic to felsic dikes, and metasedimentary quartzite.